Featured in Physics

In situ Tuning of the Electric-Dipole Strength of a Double-Dot Charge Qubit: Charge-Noise Protection and Ultrastrong Coupling

P. Scarlino,[1,2,†] J. H. Ungerer,[1,3,†] D. J. van Woerkom,[1,*] M. Mancini,[1] P. Stano,[4,5,6] C. Müller,[7] A. J. Landig,[1] J. V. Koski,[1,*] C. Reichl,[1] W. Wegscheider,[1] T. Ihn,[1] K. Ensslin,[1] and A. Wallraff[1,8]

[1]*Department of Physics, ETH Zurich, CH-8093 Zurich, Switzerland*
[2]*Institute of Physics, Ecole Polytechnique Fédérale de Lausanne, CH-1015 Lausanne, Switzerland*
[3]*Swiss Nanoscience Institute and Department of Physics, University of Basel, CH-4056 Basel, Switzerland*
[4]*RIKEN Center for Emergent Matter Science (CEMS), Wako, Saitama 351-0198, Japan*
[5]*Department of Applied Physics, School of Engineering, University of Tokyo, 7-3-1 Hongo, Bunkyo-ku, Tokyo 113-8656, Japan*
[6]*Institute of Physics, Slovak Academy of Sciences, 845 11 Bratislava, Slovakia*
[7]*IBM Quantum, IBM Research–Zurich, CH-8803 Rüschlikon, Switzerland*
[8]*Quantum Center, ETH Zurich, 8093 Zurich, Switzerland*

(Received 26 October 2021; revised 3 April 2022; accepted 26 May 2022; published 7 July 2022)

Semiconductor quantum dots in which electrons or holes are isolated via electrostatic potentials generated by surface gates are promising building blocks for semiconductor-based quantum technology. Here, we investigate double-quantum-dot (DQD) charge qubits in GaAs capacitively coupled to high-impedance superconducting quantum interference device array and Josephson-junction array resonators. We tune the strength of the electric-dipole interaction between the qubit and the resonator *in situ* using surface gates. We characterize the qubit-resonator coupling strength, the qubit decoherence, and the detuning noise affecting the charge qubit for different electrostatic DQD configurations. We find all quantities to be systematically tunable over more than one order of magnitude, resulting in reproducible decoherence rates $\Gamma_2/2\pi < 5$ MHz in the limit of high interdot capacitance. In the opposite limit, by reducing the interdot capacitance, we increase the DQD electric-dipole strength and, therefore, its coupling to the resonator. Employing a Josephson-junction array resonator with an impedance of approximately 4 kΩ and a resonance frequency of $\omega_r/2\pi \sim 5.6$ GHz, we observe a coupling strength of $g/2\pi \sim 630$ MHz, demonstrating the possibility to operate electrons hosted in a semiconductor DQD in the *ultrastrong-coupling regime* (USC). The presented results are essential for further increasing the coherence of quantum-dot-based qubits and investigating USC physics in semiconducting QDs.

DOI: 10.1103/PhysRevX.12.031004

Subject Areas: Mesoscopics, Quantum Physics
Quantum Information

I. INTRODUCTION

The semiconductor material platform [1,2] promises scalable realizations of quantum bits (qubits) with long coherence time, fast operation, and a wide range of tunability [3]. Electrons and holes are confined on small islands, called quantum dots (QDs), defined by electrostatic gates fabricated on top of semiconducting host materials [1,4,5]. QD devices can be studied directly in transport or remotely by a nearby charge detector, such as a quantum point contact or another quantum dot [1]. Recently, semiconducting QDs have also been successfully embedded in circuit quantum electrodynamics (cQED) architectures, enabling the study of double [6,7] and triple quantum dots [8] via their electric dipolar interaction with a microwave resonator. Strong coupling between resonator microwave photons and charge [9–11] and spin [8,12,13] degrees of freedom in the QDs has been achieved. Although the spin degree of freedom is of particular interest for quantum information applications, charge noise in the host substrate remains a major limitation [14,15]. Even operation of the quantum devices at sweet spots—configurations in the parameter space where critical system properties are minimally affected by noise in the control parameters [16–21]—can mitigate its effects only to a limited extent. Therefore, understanding and improving the coherence and control of the charge degree of freedom in semiconductor

[*]Present address: Microsoft Quantum Lab Delft, Delft, 2600 GA, Netherlands.

[†]These authors contributed equally to this work.

systems is of special interest also for future spin qubit applications. In fact, all recent successful cQED implementations of spins of electrons confined in QDs [8,12,13] rely on coupling the spin to the electric field of microwave photons via a controlled hybridization of the spin and orbital degrees of freedom, in effect allowing the spin qubit to acquire an electric-dipole moment. The strength of this dipole coupling can be tuned by controlling the spin-orbit degree of hybridization. This allows one to find a compromise between a charge qubit with a short coherence but large coupling to cavity photons and the more protected pure spin qubit with small or negligible coupling to cavity photons [22].

In this paper, we describe a strategy to systematically tune the double-quantum-dot (DQD) electric-dipole strength which controls the coupling rate between the DQD charge system and a superconducting microwave resonator. The approach is based on altering the magnitude of the DQD interdot capacitance while maintaining the interdot tunneling rate close to the resonator frequency. We explore different configurations of the DQD confinement potential created by the surface metallic depletion gates and demonstrate how to efficiently assess the magnitude of the DQD dipole strength in a given configuration. As we explain in Sec. II, increasing the interdot capacitance lowers the electric-dipole strength of the DQD.

In this paper, we present experiments on two distinct devices [reported in Figs. 1(a), 1(c), 1(d), and 1(e) and Figs. 1(b), 1(e), 1(f), and 1(g), respectively] with which we explore a range of the DQD electric-dipole strengths and analyze the DQD decoherence, sensitivity to charge noise, and coupling to the resonator.

In a set of experiments performed with the first device, we systematically decrease the DQD electric-dipole strength by exploring regimes in which the interdot mutual capacitance C_m becomes the dominant contribution to the DQD capacitance. In all of these DQD configurations, the DQD-cavity system is in the strong-coupling regime, namely, in a configuration where the coupling strength between the radiation and the quantum two-level system (g) exceeds the total decoherence of the coupled systems.

In the first device [see Figs. 1(a), 1(c), 1(d), and 1(e)], the DQD is coupled to a superconducting quantum interference device (SQUID) array resonator. We systematically decrease the DQD electric-dipole strength by exploring regimes with increasing interdot mutual capacitance C_m. This allows us to generate a high degree of resilience against charge noise. We make extensive use of the frequency tunability of the SQUID-array resonator [see Figs. 1(a) and 1(d)]. We reproducibly achieve a decoherence rate of only a few megahertz for DQD charge qubits in GaAs/AlGaAs operated in the tens of electrons regime [23], which substantially increases the visibility of the vacuum Rabi mode splitting for a DQD-resonator hybrid device, essential for spectroscopic characterization of the coherent electron-photon hybridization. Furthermore, we show that the reduced sensitivity to charge noise also considerably increases the qubit coherence even at finite DQD detuning.

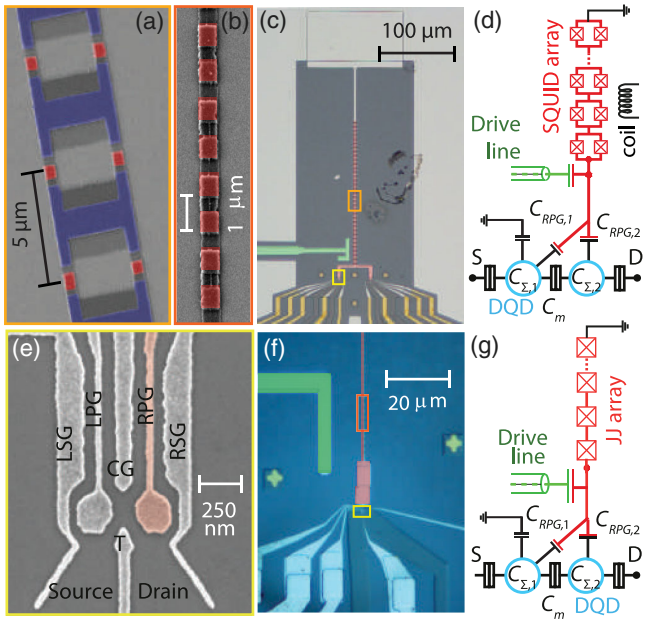

FIG. 1. Simplified circuit diagram and micrographs of the devices. (a) [(b)] False-colored SEM micrograph of a section of the SQUID [Josephson-junction] array resonator indicated by the light [dark] orange rectangle in (c) [(f)]. Josephson junctions in the array are highlighted in red. (c) False-colored optical micrograph of the measured device described in Sec. II, with a SQUID array resonator (red), ground plane (light gray), fine (light gray), and coarse (gold) gates defining the DQD. (d) [(g)] Schematic of the device and control line indicating a simplified circuit diagram of the SQUID [Josephson-junction] array resonator (red), drive line (green), the DQD (cyan), and an external coil (black). $C_{\mathrm{RPG},2}$, $C_{\mathrm{RPG},1}$, $C_{\Sigma,2}$, $C_{\Sigma,1}$, and C_m are the capacitance between the QD_2 [QD_1] and the resonator, total capacitance of QD_2 [QD_1], and interdot capacitance, respectively. (e) Scanning electron micrograph of the areas indicated by yellow rectangles in (c) and (f) showing the DQD fine gates (light gray) on the GaAs mesa (dark gray). The plunger gate galvanically connected to the resonator is highlighted in red. (f) False-colored optical micrograph of the measured device described in Sec. III, showing the substrate (dark blue), the superconducting structures including the Al fine gate forming the DQD (light blue), the Josephson-junction array (red), and the microwave feedline (green).

In the second device, a DQD is coupled to a Josephson-junction array resonator [see Figs. 1(b), 1(e), 1(f), and 1(g)]. We explore the same tuning strategy of the DQD confinement potential as used in the first device but aiming for maximizing the DQD electric-dipole strength. We increase the coupling rate of the DQD to the microwave resonator and approach the ultrastrong-coupling (USC) regime [24–26]. The USC is a configuration where the vacuum Rabi frequency (g) becomes an appreciable fraction of the uncoupled eigenfrequencies of

the system (ω_r and ω_q), frequently characterized by the ratio $g/\omega_r \geq 0.1$. In contrast to standard cavity-QED scenarios, in the USC regime the routinely invoked rotating-wave approximation is no longer applicable, and the antiresonant terms become significant [25,26]. Given the small electric-dipole moment and high decoherence rates, reaching the USC regime with a semiconductor DQD system is more demanding than with superconducting qubits. Here, we demonstrate that careful design and tuning of the DQD confinement potential and using a junction array resonator with a characteristic impedance of approximately 4 kΩ allows us to reach a coupling strength of $g/2\pi \sim 600$–650 MHz at a resonator frequency of $\omega_r/2\pi \sim 5.6$ GHz.

The article is structured as follows: In Sec. II, we discuss the DQD charge qubit and derive its sensitivity to applied voltages and charge fluctuations, which is central to the understanding of the experiments presented in later sections. In Sec. III, we present measurements aimed at maximizing the coherence of semiconductor charge qubits. In Sec. IV, we demonstrate that we can reach ultrastrong coupling to a superconducting resonator in a device with an identical quantum dot design. We conclude with Sec. V, where we give an outlook toward future research enabled by our results. Technical details, derivations, and supporting measurements are discussed in the Appendixes.

II. DOUBLE-QUANTUM-DOT CHARGE QUBIT

In this work, we consider a DQD charge qubit [4] coupled to a microwave resonator. We investigate its coherence properties and coupling strength when systematically varying the electrostatic properties of the dots. The qubit is modeled with a Hamiltonian characterized by two parameters, the detuning between the two dots ϵ and the tunneling amplitude Δ coupling them:

$$H_q = \frac{1}{2}(\epsilon\sigma_z + \Delta\sigma_x) \equiv \frac{1}{2}\hbar\omega_q \boldsymbol{\sigma}\cdot(\cos\varphi, 0, \sin\varphi). \quad (1)$$

Here, we introduce the mixing angle through $\tan\varphi = \epsilon/\Delta$, the qubit energy $\hbar\omega_q = \sqrt{\epsilon^2+\Delta^2}$, and the vector of Pauli matrices $\boldsymbol{\sigma}$. The Hamiltonian is written in the basis of position states $|l\rangle$ and $|r\rangle$, which differ in their charge configuration by a single electron transferred across the double dot. The finite overlap of these position states results in the tunneling amplitude Δ, and their energy difference defines the detuning $\epsilon = \epsilon_r - \epsilon_l$.

The DQD is defined through electrostatic gates controlled via applied voltages. Its states can be characterized by the number of charges in each dot. We define a vector of charges $\mathbf{q} = -e(n_1, n_2)^T$ and gate voltages $\mathbf{v}$. The latter leads to induced gate charges on each dot through $\mathbf{q}_G = -e(n_{G,1}, n_{G,2})^T = -e\mathbb{C}_G\mathbf{v}$, with the gate capacitance matrix $\mathbb{C}_G$ and the electron charge e (for details, see Appendix C). For a given charge-voltage configuration, the electrostatic energy of the DQD results to [1]

$$E(n_1, n_2, \mathbf{v}) = \frac{1}{2}(\mathbf{q}-\mathbf{q}_G)^T \cdot \mathbb{C}_D^{-1} \cdot (\mathbf{q}-\mathbf{q}_G). \quad (2)$$

Here, we introduce the DQD capacitance matrix

$$\mathbb{C}_D = \begin{pmatrix} C_{\Sigma,1} & -C_m \\ -C_m & C_{\Sigma,2} \end{pmatrix}, \quad (3)$$

with the total capacitance of the kth dot $C_{\Sigma,k}$ and the mutual interdot capacitance C_m. In particular, the mutual capacitance C_m is a parameter which is experimentally tunable through modifications of the shape and distance of the two dots.

The detuning ϵ in the Hamiltonian is defined as the energy difference between two states whose charge configuration differs by a single charge on either the left or right dot. We can, thus, write

$$\begin{aligned}\epsilon &= E(n_1, n_2, \mathbf{v}) - E(n_1-1, n_2+1, \mathbf{v}) \\ &= E_{C,1}(2n_1 - 2n_{G,1} - 1) - E_{C,2}(2n_2 - 2n_{G,2} + 1) \\ &\quad + 2E_{C,m}(n_2 - n_{G,2} - n_1 + n_{G,1} + 1), \end{aligned} \quad (4)$$

where we define the charging energies $E_{C,1/2} = e^2 C_{\Sigma,2/1}/[2(C_{\Sigma,1}C_{\Sigma,2} - C_m^2)]$ and $E_{C,m} = e^2 C_m/[2(C_{\Sigma,1}C_{\Sigma,2} - C_m^2)]$. To elucidate the effect of variations and fluctuations in gate voltages δV_G on the Hamiltonian parameters, we define the induced variation in gate charge as $\delta\mathbf{q}_G = \delta V_G (C_{G,1}, C_{G,2})^T$. From Eq. (4), we then find the change in ϵ to be

$$\begin{aligned}\delta\epsilon &= 2\delta V_G[C_{G,1}(E_{C,1} - E_{C,m}) - C_{G,2}(E_{C,2} - E_{C,m})]/e \\ &\approx \frac{e\delta V_G}{C_\Sigma + C_m}(C_{G,1} - C_{G,2}), \end{aligned} \quad (5)$$

where in the last step we assume equal QDs with $C_{\Sigma,1} = C_{\Sigma,2} = C_\Sigma$. The generalization of Eq. (5) to the case of dissimilar QDs is given in Appendix C.

We show that qubit electrical sensitivity, expressed in Eq. (5), appears as an essential parameter for both qubit-resonator coupling and coherence. Let us, therefore, analyze Eq. (5) in more detail. It states that the sensitivity to a given gate voltage is larger if the two dots are coupled to it differently, $C_{G,1} \neq C_{G,2}$, and is smaller if the dot mutual capacitance C_m grows. The more tightly the two dots are coupled, the less differently they respond to a voltage change on a gate and the smaller is the DQD effective dipole strength. This finding is a central point of this paper.

On the first look, Eq. (5) suggests a reduction in electrical sensitivity by $1/(C_\Sigma + C_m)$. However, the reduction is stronger, due to a sum rule that the capacitances need to satisfy. To see that, we write a single-dot total capacitance as

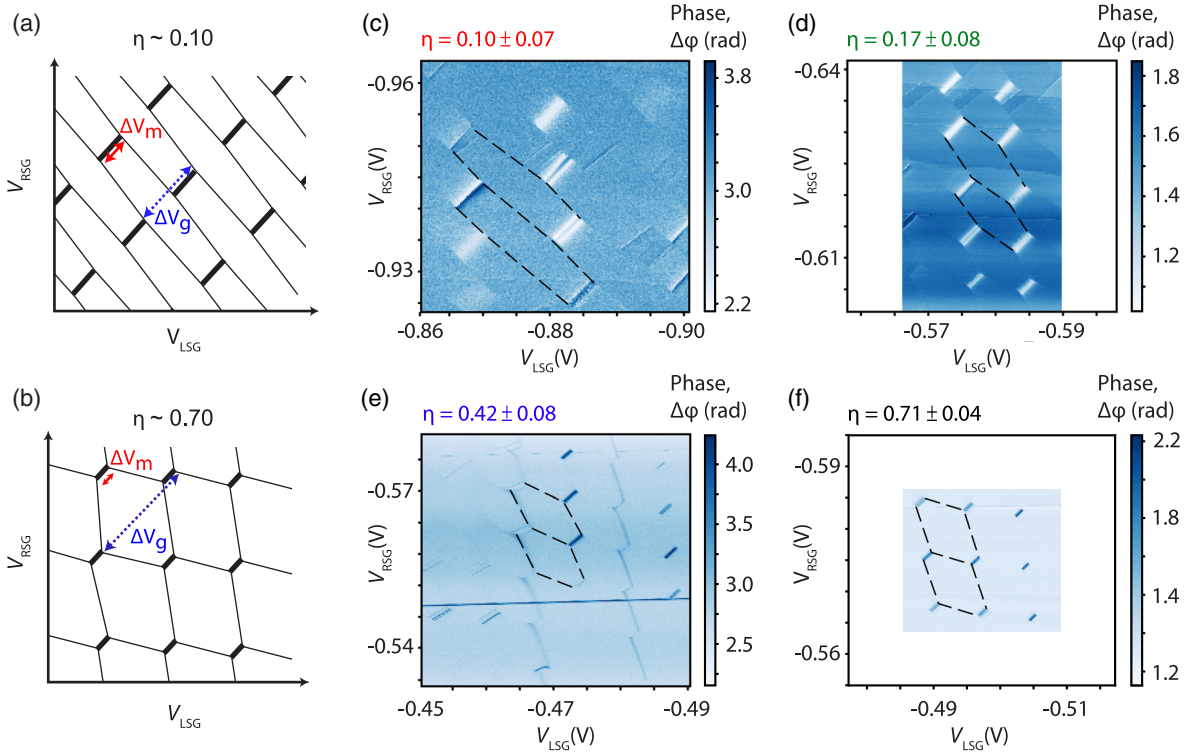

FIG. 2. DQD charge stability diagrams. (a) A schematic of a DQD charge stability diagram for a configuration with a large mutual capacitance C_m, resulting in $\eta \sim 0.10$. The black areas (lines) represent interdot (QD_i-$lead_i$) charge degeneracy regions. The dipole strength η is determined directly from the charge stability diagrams. ΔV_m and ΔV_g are the voltage distance between the two triple points and QD-lead energy degeneracies, respectively. (b) The same as (a) but for smaller C_m, resulting in $\eta \sim 0.70$. (c)–(f) Measured DQD charge stability diagrams obtained for four different DQD configurations in correspondence of four distinct values of C_m [decreasing from (c) to (f)]. Each charge stability diagram is measured by monitoring the change in the phase $\Delta\phi$ of the resonator reflectance in response to the DQD gate voltages. The axes scales of the LSG and RSG gate voltages are kept the same in the four panels for ease of comparison.

$$C_\Sigma = C_m + C_{\mathrm{gnd}} + \sum_g C_g = C_m + C_{\mathrm{out}}, \tag{6}$$

where we define its capacitance to ground as C_{gnd} and to each gate as C_g. We also use C_{out}, the capacitance to the outside world, as the total capacitance to everything else except the other single dot. With this notation, we write the variation of ϵ due to an applied voltage δV_G as

$$\delta\epsilon = e\delta V_G \frac{C_{G,1} - C_{G,2}}{C_{\mathrm{out}}} \frac{C_\Sigma - C_m}{C_\Sigma + C_m}. \tag{7}$$

Here, we interpret the last term as the renormalization factor for the dipolar energy of the system (see Appendix B)

$$\eta = \frac{C_\Sigma - C_m}{C_\Sigma + C_m} = \frac{1 - C_m/C_\Sigma}{1 + C_m/C_\Sigma}. \tag{8}$$

If the dots have nonequal total capacitance ($C_{\Sigma,1} \neq C_{\Sigma,2}$), an additional contribution appears in Eq. (7). However, the definition of the factor η given in Eq. (8) remains the same; see Appendix C for details. In the rest of the paper, we refer to η as *dipole strength* for brevity. The quantities defining the dipole strength as given in Eq. (8) can be directly read off the standard charging diagram of the double dot as illustrated in Figs. 2 and 7.

Note that here we are not considering the concomitant change in tunneling amplitude Δ when changing the electrostatic confinement of the dot. This is because the lever arm for changing the tunneling amplitude Δ in GaAs QDs similar to the one considered here is typically at least one order of magnitude smaller than for changes in ϵ [27]. Furthermore, in the experiments presented here, through independent tuning of the T and CP gate voltages [see Fig. 1(e)], we take care to keep Δ/h around 4.5–5.5 GHz in all measurements (see Table I). In this way, we can specifically investigate changes in the DQD coherence properties and coupling strength when tuning mainly the interdot capacitance C_m and, therefore, only the dipole strength η.

Equations (7) and (8) allow a straightforward derivation of the interaction between the charge qubit and the resonator by replacing the voltage fluctuations δV_G by the voltage vacuum fluctuations of a superconducting

resonator of frequency $\omega_r = 1/\sqrt{L_r C_r}$, given by its capacitance C_r and inductance L_r:

$$\delta V_G = \sqrt{\frac{\hbar\omega_r}{2C_r}}(a + a^\dagger). \tag{9}$$

a is the annihilation operator of the resonator quantized electromagnetic field. The strength of the resulting qubit-resonator interaction $H_{q-r} = (1/2)g\sigma_z(a + a^\dagger)$ can be parametrized using the resonator impedance $Z_r = \sqrt{L_r/C_r}$ as

$$g = \omega_r\sqrt{\frac{2e^2}{\hbar}Z_r} \times \eta\frac{C_{G,1} - C_{G,2}}{C_{\text{out}}}, \tag{10}$$

separating the contributions from the resonator and the DQD charge qubit. Since instrumental constraints limit the resonator frequency, the crucial resonator parameter when aiming at maximizing the coupling strength is its impedance Z_r. The dot properties and system geometry enter through the second term.

Equation (5) also encodes the qubit coupling to electrical noise. To describe electrical noise, we consider uncontrolled fluctuations of voltage V_G, causing random fluctuations of the qubit energy and, thus, decoherence. The latter is a complex process, depending on the details of the time correlations in these fluctuations. After analyzing most typical scenarios [28], which we list in Appendix D, here we restrict ourselves to dephasing due to singular noise with a $1/f$-type spectral function $S(\omega) = A/|\omega|, \omega_{\text{ir}} < \omega < \omega_c$, linearly coupled to the qubit. The low- and high-frequency cutoffs ω_{ir} and ω_c are typically defined through experimental timescales. In the quasistatic approximation, where the noise is considered static in each individual run of the experiment, this leads to decay of the qubit off-diagonal density matrix element with a Gaussian form [28] as

$$\begin{aligned}\ln c_{\text{lin}}^{1/f}(\tau) &= -\tau^2\left(\frac{\partial\hbar\omega_q}{\partial\epsilon}\right)^2\left(\frac{\partial\epsilon}{\partial V_G}\right)^2 A\ln\left(\frac{\omega_c}{\omega_{\text{ir}}}\right)\\ &\equiv -\tau^2\left(\frac{\partial\hbar\omega_q}{\partial\epsilon}\right)^2\sigma_\epsilon^2 \equiv -(\Gamma_\varphi\tau)^2.\end{aligned} \tag{11}$$

Here, τ denotes the evolution time, and $c(\tau)$ is the decay envelope. Introducing the pure dephasing time Γ_φ, the expression can be written as a function of a dimensionless parameter $\Gamma_\varphi\tau$. Additionally, the noise parameter $\sigma_\epsilon \propto \partial\epsilon/\partial V_G$, given by Eq. (5), isolates the effects that are in our focus. Finally, the noise of semiconducting charge qubits is most probably not dominated by fluctuating voltages of the gates but fluctuating charges of impurities. We show in Appendix C that there is a relation analogous to Eq. (7) describing detuning response to charge impurity fluctuations.

The dipole strength as defined in Eq. (8) is experimentally easily accessible and provides useful qualitative predictions. Indeed, from Eq. (10), we see that the coupling to the resonator theoretically scales proportionally to η. Maximizing the coupling, therefore, calls for maximizing η, i.e., minimizing the mutual capacitance of the two dots. If the coherence of the DQD charge system is limited by electric noise-induced dephasing, the coherence time $1/\Gamma_2 \sim 1/\Gamma_\phi$ is, according to Eq. (11), expected to scale as $1/\eta$, since Eqs. (7) and (8) give $\partial\epsilon/\partial V_G \sim \eta$. Therefore, a maximally coherent charge qubit requires minimizing η. The scaling $1/\eta$ is a consequence of the singular noise resulting in a Gaussian decay form. Other relevant decay channels, like relaxation and nonsingular noise, lead to a scaling of the coherence time as $\propto 1/\eta^2$ (see Table III in Appendix D) [28]. We thus expect that, depending on the details of the dominant noise source in the experiments, the qubit coupling quality factor $Q = g/\Gamma_2$ is either constant as a function of η (for singular noise dominating dephasing) or can be $\propto 1/\eta$ (for regular dephasing noise or if relaxation dominates). The latter situation allows one to optimize Q by tuning the mutual dot capacitance. In the following Sec. III, we investigate which specific scenario is realized in our system. We find that the charge-photon coupling strength g and decoherence rate Γ_2 are both *in situ* tunable over an order of magnitude, while Q remains approximately constant. Minimizing the dipole strength, we achieve $\Gamma_2/2\pi < 5$ MHz. In Sec. IV, aiming at maximizing the charge-photon coupling strength g, we employ a resonator with an even larger impedance. Making use of both terms in Eq. (10), we achieve charge-photon coupling strength $g/2\pi \sim 630$ MHz for a fundamental mode resonator frequency of $\omega_r/2\pi \sim 5.6$ GHz.

III. INCREASING CHARGE QUBIT COHERENCE

In this section, we describe experiments performed on the first device where we investigate a GaAs DQD charge qubit strongly coupled to a SQUID array resonator [see Figs. 1(a), 1(c), 1(d), and 1(e)] [10,23]. We characterize the qubit coherence properties and its coupling strength g to the resonator. Aiming to reduce decoherence of the qubit, we *in situ* explore different electrostatic confinement potentials of the DQD in the few-electron regime (approximately 10–20) obtained by tuning the voltages applied to the electrostatic gates defining the DQD [see Fig. 1(e)]. Each configuration leads to a different strength of the effective dipole interaction between the DQD and resonator, characterized by a different dipole strength η as defined in Eq. (8).

We use a GaAs/AlGaAs heterostructure with a 2DEG approximately 90 nm below the surface. Depletion gates are used to define the DQD electrostatic potential. The right dot plunger gate is galvanically connected to the resonator [see Figs. 1(c) and 1(e)]. We measure the resonator response in reflection via the drive line [indicated in green in Fig. 1(c)] in a heterodyne detection scheme by monitoring the amplitude ($|S_{11}|$) and phase difference ($\Delta\phi = \text{Arg}[S_{11}]$) of the

reflected signal [29]. An additional spectroscopy tone can be applied through the same line. The second DQD in the device [Fig. 1(c)] is tuned deeply into Coulomb blockade and does not participate in the reported experiment.

The impedance of the employed SQUID array resonator [see Figs. 1(a) and 1(c)] is estimated to be $Z_r^{\mathrm{Sq}} = \sqrt{L_{\mathrm{Sq}}/C_{\mathrm{Sq}}} \sim 1$ kΩ. Similar high-impedance resonators have been previously shown to enable the strong-coupling regime between a DQD and microwave photons [10]. A magnetic flux, applied via a superconducting coil mounted on the sample box, is used to tune the resonator in the frequency range $\omega_r/2\pi \sim [4.2, 5.7]$ GHz (see Table I). The internal resonator dissipation κ_{int} and coupling to the microwave feedline κ_{ext} change with the resonator frequency, as shown in Fig. 6(c) in Appendix A [30].

The DQD response to the gate voltages is characterized by charge stability diagrams [4], which we measure by recording the amplitude and phase response of the reflectance of the resonator [6]. From those diagrams, we extract the charging energies and capacitances of the DQD. In Figs. 2(c)–2(f), we present four typical examples of DQD charge stability diagrams realized within the same device by *in situ* tuning the voltages on the four gates defining the DQD [Fig. 1(e)]. The differences between the four configurations lie mainly in different voltages applied to the gates T and CG [cf. Fig. 1(e)] which control the interdot tunnel barrier and are listed in Table II in Appendix A. For ease of comparison, the axis scales are identical for the four panels in Fig. 2. We highlight that these four different configurations present similar interdot tunneling amplitudes Δ despite the different gate voltage values (see Table I in Appendix A).

Comparing the four DQD configurations shown in Figs. 2(c)–2(f), we notice that the average spacing between the DQD triple points [4] [maximal in Fig. 2(c)] decreases relative to the spacing between two consecutive QD-reservoir charge transitions [dashed lines in Figs. 2(c)–2(f)]. This variation can be interpreted as a change in the contribution of the interdot coupling capacitance (C_m) to the total capacitance of the individual QDs ($C_{\Sigma,1}$ and $C_{\Sigma,2}$) [4]. This translates into the dipole strength η [Eq. (8)] covering the interval [0.1, 0.7] in our experiments. Both C_m/C_Σ and the dipole strength η can be determined from the charge stability diagrams by considering the arrows indicated in the schematics in Figs. 2(a) and 2(b). The red arrow represents the distance of two adjacent DQD triple points, and the blue arrow connects two consecutive electron transitions with the leads. As derived in Appendix A, in the simplified case of symmetric QDs, $C_{\Sigma,1} = C_{\Sigma,2} = C_\Sigma$, and neglecting gate-cross capacitances, one finds $C_m/C_\Sigma = \Delta V_m/(\Delta V_g - \Delta V_m)$ and $\eta = 1 - [(2\Delta V_m/\Delta V_g)]$. ΔV_m (ΔV_g) represents the length of the red (blue) arrow in Figs. 2(a) and 2(b). Furthermore, we emphasize that this striking change of the DQD interdot capacitance is obtained while keeping the interdot tunneling rate in the range 4 GHz $< \Delta/h <$ 6 GHz. The ability to control Δ and η independently allows us to probe the interaction with the resonator in both resonant and dispersive regimes.

In total, we study 11 different DQD configurations from which we extract the parameters summarized in Table I. For three of these configurations, we present in Fig. 3 the hybridized qubit-resonator energy spectrum [see Figs. 3(a)–3(d)], a measurement of the intrinsic DQD charge qubit linewidth [see Fig. 3(e)], and a measurement of the root-mean-square amplitude of the detuning noise σ_ϵ defined in Eq. (11) [see Fig. 3(f)]. The data plotted in Figs. 3(d) and 3(e) are taken at charge degeneracy ($\epsilon = 0$).

In Figs. 3(a)–3(c), we show three examples of hybridized spectra in the strong-coupling regime for different dipole strengths. The DQD stability diagrams of the three configurations in Figs. 3(a)–3(c) are shown in Figs. 2(e), 2(d), and 2(c), respectively, in corresponding colors. We tune the DQD gate voltages and the SQUID array resonance frequency to reach the resonance condition $\omega_q = \omega_r$ at approximately zero detuning ϵ. Varying the DQD detuning, we observe the characteristic shifts in the dispersive regime and clear indications of an avoided crossing [9,10] at resonance. We analyze the hybridized spectrum and extract the coupling strength g, resonator resonance frequency $\omega_r/2\pi$, and DQD tunneling amplitude Δ by fitting the observed resonances to the spectrum extracted from the system Hamiltonian (see Appendix F for details). The Hamiltonian spectrum is plotted by dashed lines in Figs. 3(a)–3(c).

When comparing these three configurations, we take note of a correlation between the coupling strength g and the visibility of the reflected signal (Rabi modes splitting) around the avoided crossing. Figure 3(d) shows the line cuts at the resonance [detuning indicated by black arrows in Figs. 3(a)–3(c)] visualizing the correlation between the coupling strength and the visibility of the Rabi modes splitting. Furthermore, increasing η, we observe a distinct increase of the linewidth of the Rabi modes [$\Gamma_R \sim (\kappa_{\mathrm{ext}} + \kappa_{\mathrm{int}})/2 + \Gamma_2$], extracted by fitting the data to a sum of two Lorentzian lines [see the solid line in Fig. 3(d)], and a clear reduction in the depth of the two Lorentzian [compare the y axis for the three panels in Fig. 3(d)]. This suggests that the dipole strength also has a strong influence on the system decoherence.

We investigate in more detail the correlations between the measured dipole strength η and the observed coherence of the charge qubit. Using two-tone spectroscopy [10,31], we measure the intrinsic qubit linewidth at charge degeneracy ($\epsilon = 0$) and its sensitivity to the noise of the detuning parameter induced by the charge noise of the DQD electromagnetic environment [32]. Measuring the power dependence of the qubit linewidth, we extract the zero power linewidth ($P_S \to 0$) [see Fig. 3(e)], from which we determine the intrinsic DQD charge decoherence rate Γ_2 [10,31]. In this experiment, we reach a DQD linewidth as low as approximately 4.5 ± 0.2 MHz for a configuration

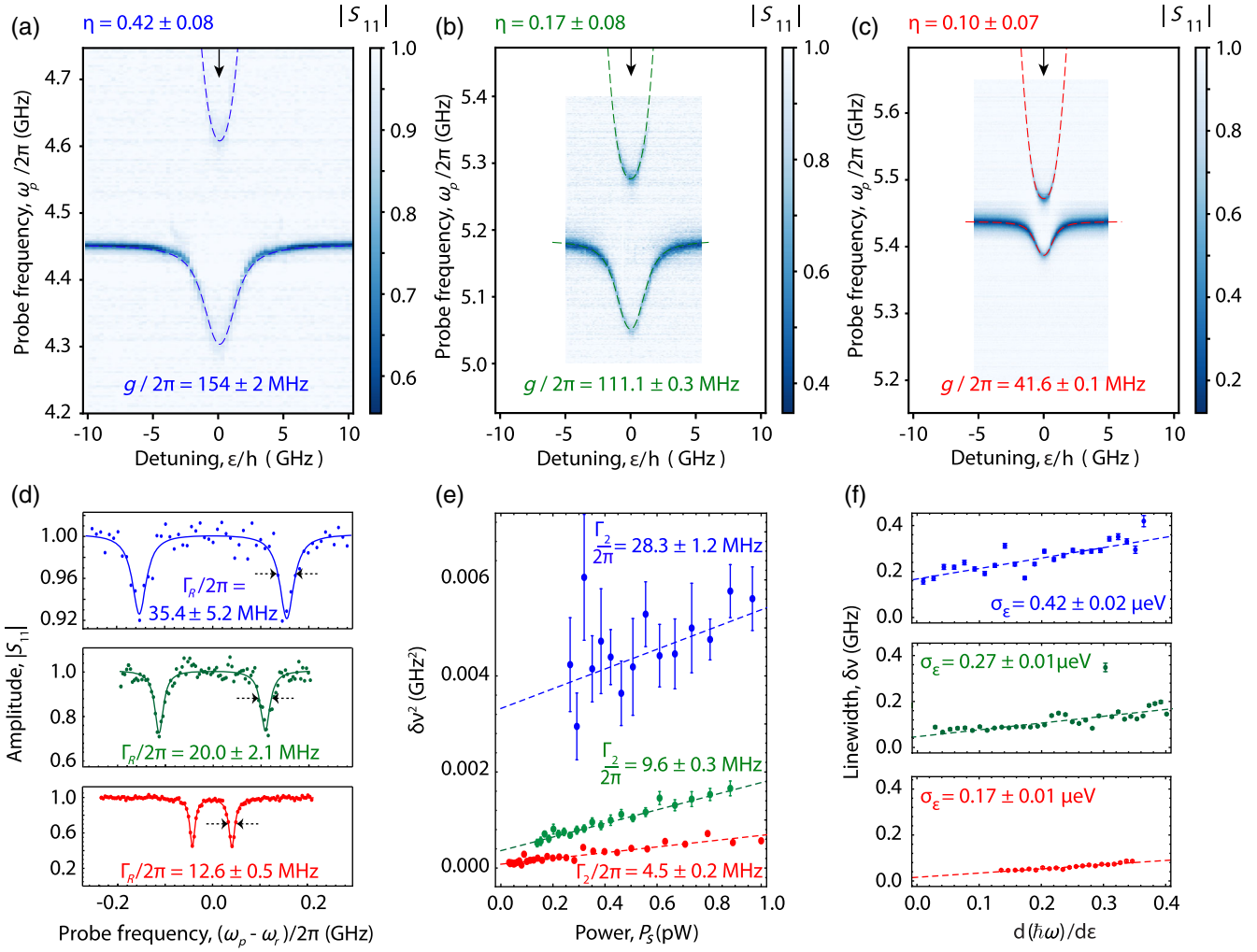

FIG. 3. The dependence of the coupling strength g and DQD coherence rates Γ_R and Γ_2 for DQD configurations with dipole strengths $\eta = 0.42, 0.17, 0.10$. (a)–(c) Resonator reflectance amplitude $|S_{11}|$ versus DQD detuning ϵ for three representative values of the dipole strength $\eta \sim 0.42 \pm 0.08$ (blue curve), $\eta \sim 0.17 \pm 0.08$ (green curve), and $\eta \sim 0.10 \pm 0.07$ (red curve) [corresponding to the DQD charge stability diagrams in Figs. 2(c), 2(b), and 2(a), respectively]. (d) Resonator amplitude response $|S_{11}|$ (dots) versus probe frequency $\omega_p/2\pi$ at $\epsilon = 0$ [see the black arrow in (a)–(c)], displaying well-resolved vacuum Rabi mode splittings. The solid line is a fit to the sum of two Lorentzian lines. The quoted Γ_R is computed as an average of the two linewidths. (e) Squared qubit linewidth $\delta\nu_q^2$ (dots) versus spectroscopy drive power P_s, measured via two-tone spectroscopy [10]. The dashed lines are linear fits. The zero-power linewidths Γ_2 are given. (f) Qubit linewidth $\delta\nu_q$ (dots) versus $d(\hbar\omega)/d\epsilon$ extracted from two-tone spectroscopy [10]. The dashed lines are linear fits. Their slopes define σ_ϵ according to Eq. (11).

with $\eta = 0.10 \pm 0.07$. In contrast, by *in situ* tuning to a configuration with $\eta = 0.71 \pm 0.03$, the DQD charge qubit linewidth increases by a factor of 8.

At $\epsilon = 0$, the charge qubit is first-order insensitive to charge noise, since $\partial\omega_q/\partial\epsilon = 0$. Measuring the dependence of the qubit linewidth against the detuning ϵ, we extract the detuning noise σ_ϵ according to Eq. (11) [see Figs. 3(f) and 4(c) and also Refs. [21,23]]. The extraction of σ_ϵ in two-tone spectroscopy is performed at a larger resonator readout power explaining the lower error bars on the extracted linewidths and the higher value of qubit linewidth at $\epsilon = 0$ compared to Fig. 3(e). We notice that σ_ϵ clearly decreases for lower η.

The measurements presented in Fig. 3 indicate that increasing the capacitance ratio C_m/C_Σ reduces the resonator-DQD coupling strength g [Fig. 3(d)], the qubit decoherence $\Gamma_2 \equiv \delta\nu(P_S \to 0)$ [Fig. 3(e)], and the sensitivity of the qubit energy to detuning noise [Fig. 3(f)] [33]. The reduced sensitivity of the DQD to charge noise is engineered through a large mutual capacitance of strongly coupled QDs.

We summarize results of similar measurements for all 11 investigated DQD configurations in Fig. 4. In order to systematically compare the coupling strength g of the different configurations, we normalize it to [34]

$$\bar{g}_\perp = g(\omega_r/2\pi = \Delta/h = 5\ \text{GHz}) = g\frac{\Delta}{\hbar\omega_r}\frac{5\ \text{GHz}}{\omega_r/2\pi}. \quad (12)$$

The normalization aims to systematically account for the small differences in the resonator frequency or inductance and in DQD tunneling amplitude Δ [10] at which the experiments are performed (see Table I and Appendix H). The normalized coupling strength $\bar{g}_\perp/2\pi$ ranges from 41.6 to 250.6 MHz. The dependence of the normalized coupling $\bar{g}_\perp$ on η agrees with the linear relation [see Fig. 4(a)] derived as Eq. (10).

A similar dependence on η is also observed for the DQD decoherence Γ_2 [Fig. 4(b)] and detuning noise σ_ϵ [Fig. 4(c)], as modeled by Eq. (11). In order to display the linear relation between coupling strength $\bar{g}_\perp$ and DQD decoherence Γ_2, we plot both quantities in Fig. 4(d). The scattered $(\Gamma_2, \bar{g}_\perp)$ data lie within the 3σ confidence interval of the linear fit. The proportionality relation is additionally highlighted by inspecting the quality factor of the resonator-qubit hybrid system $Q = \bar{g}_\perp/\Gamma_2$ [35]. In Fig. 4(e), we observe that Q does not show a strong dependence on the dipole strength η, but it is scattered around a mean value of 9.7 with a standard deviation of 2.2, indicating that the coherence of the system is likely dominated by dephasing due to singular charge noise (see Sec. I).

For a circuit QED architecture realized with semiconductor QDs and superconducting resonators, the strong-coupling regime has been reached only recently [9,10]. Intrinsic limitations are the high decoherence rate of the orbital-charge degree of freedom and the small

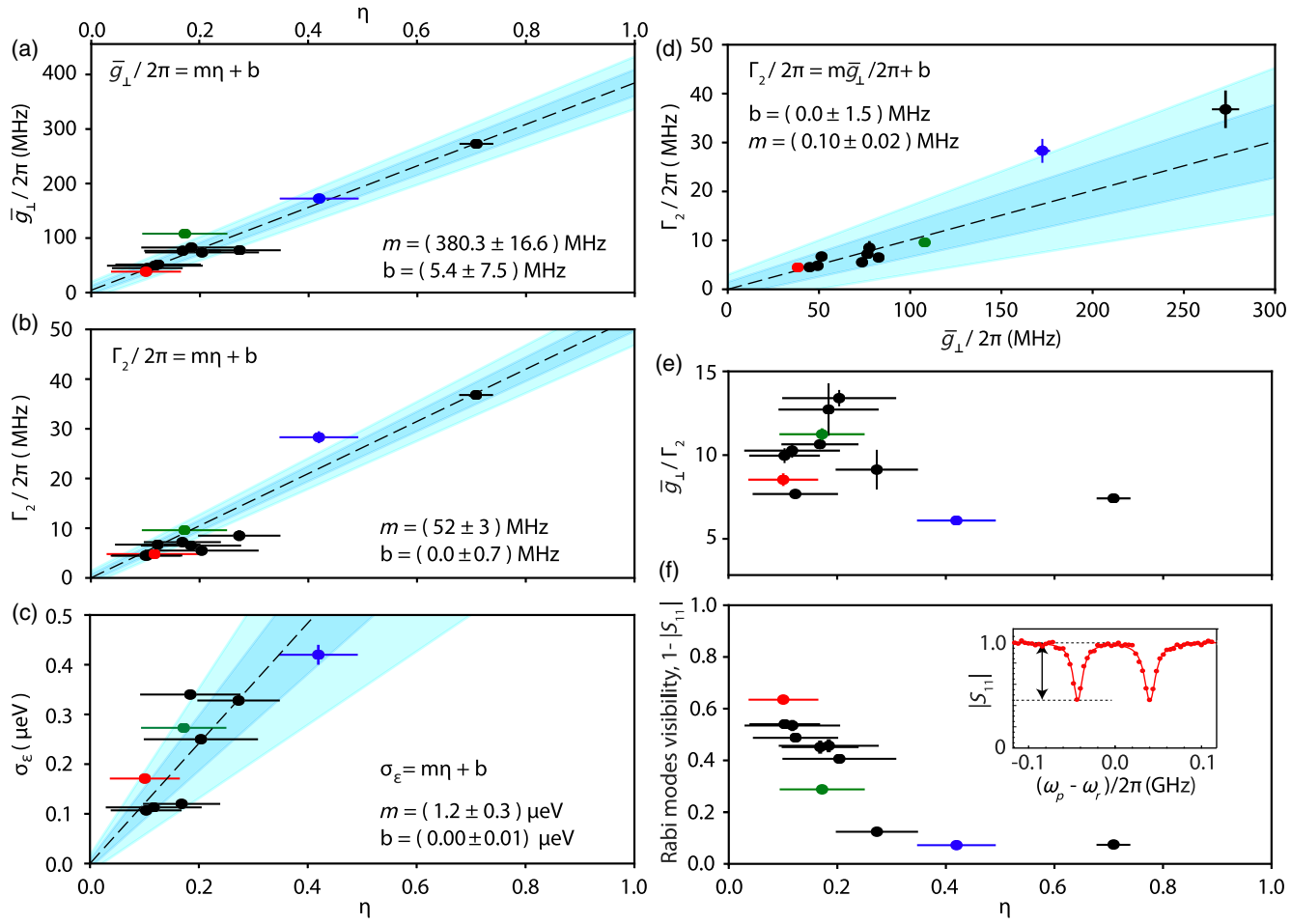

FIG. 4. Coupling strength and decoherence parameters extracted for 11 DQD gate bias voltage configurations. (a) Normalized coupling $\bar{g}_\perp$ [see Eq. (12)] of the DQD charge qubit to the resonator versus the dipole strength η. (b) Qubit linewidth Γ_2 versus η. The linewidth is extracted as in Fig. 3(e). (c) Effective detuning noise of the DQD charge qubit σ_ϵ versus η, obtained as in Fig. 3(f). For two configurations in correspondence with $\eta = 0.123$ and 0.709, we cannot extract σ_ϵ due to either spurious resonances or enhanced sensitivity to detuning noise, respectively. (d) DQD linewidth Γ_2 versus the normalized coupling. The data in (a)–(d) are fitted to a linear model plotted as dashed lines, and the fit parameters are stated in the panels. The dark [light] blue area represents the one- [two-]sigma confidence interval. (e) The quality factor $\bar{g}_\perp/\Gamma_2$ versus η. (f) Visibility of the vacuum Rabi modes (at resonance) $(1 - |S_{11}|) = 2\kappa_{\text{ext}}/(\kappa_{\text{ext}} + \kappa_{\text{int}} + 2\Gamma_2)$ versus η. The inset shows an example of a vacuum Rabi mode splitting, with the black arrow indicating the visibility of a Rabi mode at the resonance.

electric-dipole moment of electrons confined in QDs. The high qubit decoherence implies low visibility of the vacuum Rabi mode splitting, even if strong coupling is reached [10]. In Appendix F 4, we derive an expression for the visibility of the vacuum-Rabi mode splitting for a single-port resonator coupled to a DQD and tested in reflection. In the case of a DQD and resonator being tuned into resonance, we find $(1-|S_{11}|)=2\kappa_{\rm ext}/(\kappa_{\rm ext}+\kappa_{\rm int}+2\Gamma_2)$. The estimated visibility is plotted in Fig. 4(f) for the different DQD configurations explored in this study. When tuning the DQD into a configuration where the interdot capacitance is the dominant contribution ($\eta\to 0$), the Rabi mode splitting visibility is considerably increased despite a reduction in the coupling strength. Furthermore, it is instructive to consider the system cooperativity, defined as $C=\bar{g}_\perp^2/[\Gamma_2(\kappa_{\rm ext}+\kappa_{\rm int})]$, representing a dimensionless measure of the light-matter interaction strength in our hybrid system. As reported in Appendix G [see Fig. 9(a)], we achieve $C>100$ by making use of the described tuning strategy for the DQD electric dipolar energy. It represents the highest cooperativity reported so far for hybrid QD-resonator systems (see Ref. [35] for a comparison), even when comparing to hybrid spin-photon systems.

To summarize this section, we realize a DQD coupled to a SQUID array resonator. We observe a striking and clear dependence of the DQD-resonator coupling strength, DQD charge decoherence rate, and DQD detuning noise on the dipole strength, parametrized by η, as defined in Eq. (8). The characterization of different DQD configurations, realized by changing *in situ* the voltages applied to the DQD depletion gates over an extensive voltage range, demonstrates the possibility to reduce the charge qubit decoherence rate down to less than 5 MHz, thanks to the reduced DQD electric-dipole strength. The improved charge coherence allows one to considerably increase the visibility of the charge qubit-resonator Rabi vacuum mode splitting at small coupling strengths (see Appendix F).

IV. ULTRASTRONG COUPLING WITH A JUNCTION ARRAY RESONATOR

In Sec. III, we investigate the possibility to *in situ* tune the DQD dipolar coupling energy. We explore the trade-off between the qubit-resonator coupling and the DQD charge decoherence rate. In this section, we show that the same strategy allows us to approach the ultrastrong-coupling regime. With this goal in mind, we realize a second device. It is similar to the first device from the DQD side, but the SQUID array resonator is replaced by a more compact Josephson-junction (JJ) array resonator [36]. Replacing SQUIDs with single Josephson junctions in the array makes the resonator fixed in frequency, reducing the flexibility on tuning parameters. On the other hand, as illustrated in Fig. 1(b) and explained in Appendix E, the change reduces the dimensions of the array unit. We, thus, achieve overall a higher total Josephson inductance with a shorter array: The length of the JJ resonator is approximately 70 μm, instead of approximately 250 μm for the SQUID array [compare Figs. 1(a) and 1(b) and Figs. 1(c) and 1(f)]. The JJ array resonator has a lower stray capacitance to ground $C_{\rm gnd}^{\rm JJ}\sim 5$ fF, with a total inductance of $L_{\rm tot}^{\rm JJ}\sim 100$ nH and, in turn, a resonator impedance $Z_r^{\rm JJ}\sim 4$ kΩ. Parameters of the SQUID and JJ arrays are compared in Table V.

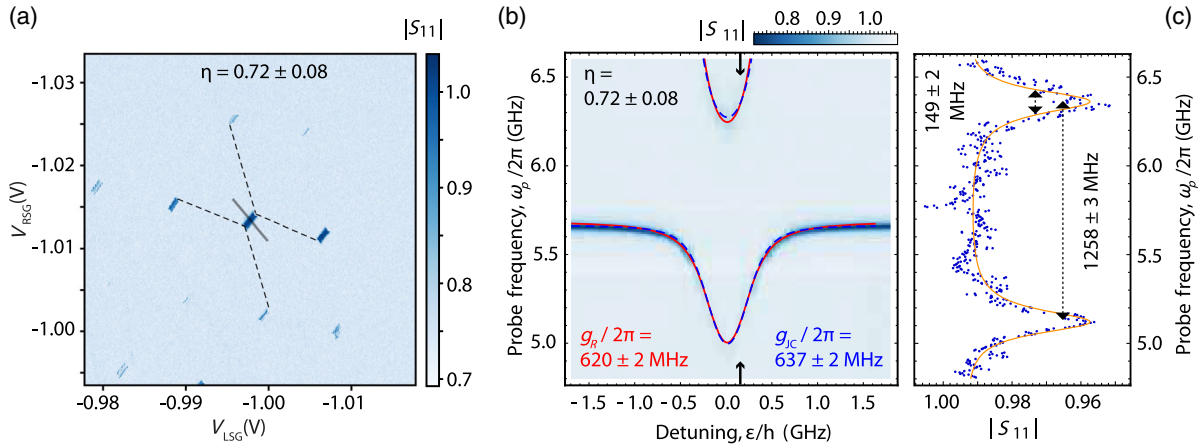

FIG. 5. Investigation of a bias configuration approaching the ultrastrong-coupling regime for a DQD coupled to a JJ array resonator. (a) Charge stability diagram of the DQD measured by monitoring the change in resonator reflectance amplitude $|S_{11}|$ for the extracted dipole strength $\eta=0.72\pm0.08$. (b) Resonator amplitude response $|S_{11}|$ taken by varying the DQD detuning ϵ along the gray line indicated in (a) by applying appropriately chosen voltages to the two side gates. The red (blue) line represents a fit to the Rabi (JC) model (see Appendix F). (c) Measured resonator reflectance $|S_{11}|$ (dots) versus probe frequency ω_p extracted at resonance for $\epsilon/h=0.15$ GHz [black arrows in (b)], displaying a vacuum Rabi mode splitting. The orange line represents a fit to a Rabi master equation model. The JJ array resonator losses are $\kappa_{\rm int}/2\pi=19.5\pm0.1$ MHz and $\kappa_{\rm ext}/2\pi=5.7\pm0.1$ MHz.

Aiming at realizing the USC regime with semiconductor quantum dots, we investigate a DQD configuration corresponding to the largest dipole strength that we are able to achieve ($\eta \approx 0.72$). As discussed in Sec. III, we detect the amplitude and phase of the signal reflected off the resonator. We configure the DQD tunneling amplitude close to $\Delta/h \sim \omega_r/2\pi$ and change the DQD detuning. Upon bringing the qubit energy into resonance with the resonator, $\omega_q \sim \omega_r$, a clear avoided crossing is observed in the resonator reflectance [see Figs. 5(b) and 13(b)]. It is a sign of reaching the strong-coupling regime.

The data are in excellent agreement with the spectrum of the hybridized system numerically calculated using g, ω_r, and Δ as adjustable parameters. We fit a Rabi (red solid line) and a Jaynes-Cummings (JC) (blue dashed line) model and present the results in Fig. 5(b). We extract coupling strength $g_R/2\pi \sim 620 \pm 2$ MHz ($g_{\mathrm{JC}}/2\pi \sim 637 \pm 2$ MHz) from which we can estimate $g_{R,\mathrm{JC}}/\omega_r \sim 0.11 \pm 0.01$, reaching the ultrastrong-coupling regime [24–26]. The discrepancy between the values obtained from the Rabi and JC fits can be explained by the onset of the USC regime as the rotating-wave approximation starts to break down [37]. The resonator reflectance $|S_{11}|$ versus probe frequency ω_p at the DQD-resonator detuning value indicated by the black arrow in Fig. 5(b) (resonant condition) is shown in Fig. 5(c). By fitting a master equation model [see the solid orange line in Fig. 5(c)] to the measured $|S_{11}|$, we extract a DQD decoherence of $\Gamma_2/2\pi \sim 149 \pm 2$ MHz and a Rabi mode splitting of $2g/2\pi \sim 1258 \pm 3$ MHz. Resolving the two dips of the vacuum Rabi mode splitting indicates that the system is still in the strong-coupling regime despite the extra decoherence introduced by the large DQD electric-dipole strength.

V. CONCLUSIONS

We have realized two hybrid devices with which we have studied charge configurations at the two extremes of the explored tunable DQD electric-dipole strength. We have demonstrated the systematic control of the DQD electric-dipole strength, allowing us to explore a broad range of different regimes in the same device. In particular, we have demonstrated that it is possible to decrease the electric dipolar coupling energy of the DQD by tuning it into a configuration in which the interdot mutual capacitance C_m becomes the dominant contribution of the total DQD capacitance. In such a configuration, the small dipole strength ($\eta \to 0$) reduces both the DQD coupling to the resonator and its decoherence rate, down to $g/2\pi \sim 40$ MHz and $\Gamma_2/2\pi < 5$ MHz, respectively.

We have made use of the DQD dipole strength control reported here to reduce the decoherence rate of DQD devices used in some of our previous works. It has led to the observation of a DQD qubit linewidth down to $\Gamma_2/2\pi \sim 3$ MHz in a similar device [23,38]. These decoherence rates are well below values reported typically for semiconductor charge qubits, usually observed to be above hundreds of megahertz or even up to several gigahertz [10,16,39]. The possibility to achieve these remarkably low decoherence rates for a DQD charge qubit enabled the realization of time-resolved dispersive readout [23], and distant qubit-qubit interaction mediated by virtual microwave photons [38,40].

Here, we have provided a detailed explanation and a method to engineer low charge decoherence by modifying the contribution of the interdot capacitance C_m to the total QD capacitance, which we can easily assess and tune by exploring the DQD stability diagram. Furthermore, this work sheds new light on the puzzling observation reported by different experiments on the QD-resonator hybrid system [23,41] which reported that g and Γ_2 can vary considerably within the same device configured in different regions of the DQD charge stability diagrams.

In addition, we show that, by using the same tuning strategy of the DQD confinement potential but striving to maximize the DQD electric dipolar coupling energy, we can considerably increase the DQD-resonator coupling strength. This is achieved by configuring the DQD gate voltages to minimize the interdot capacitance C_m. To further increase the coupling strength, we implemented a more compact Josephson-junction array resonator with reduced stray capacitance with respect to a SQUID array resonator. This results in a $Z_r^{\mathrm{JJ}} \sim 4$ kΩ resonator impedance. The JJ array resonator enabled a maximum coupling of $g/2\pi \sim 630$ MHz for a fundamental mode resonator frequency of $\omega_r/2\pi \sim 5.6$ GHz. In this way, we realize the ultrastrong-coupling regime between electrons hosted in a semiconductor DQD and a microwave resonator. By increasing the resonator impedance even further and by defining DQDs in shallower 2DEGs, or in semiconductor nanowires and Si-CMOS devices, where a higher gate lever arm (up to 0.75 in Ref. [42]) has been demonstrated for QDs, it may well be possible to achieve $g/\omega_r \sim 0.4$–0.5. This could enable more advanced investigations of the effects of the breakdown of the rotating-wave approximation in this class of light-matter hybrid devices [24–26].

Recent experiments with holes confined in 2D-Ge heterostructures have reported effective charge and gate noise lower by a factor of 2–4 with respect to Si and GaAs 2DEG systems [43], estimated by recording the current fluctuations of a charge detector over long waiting times. Applying the dipole strength tuning strategy described in this paper to holes confined in QDs defined in 2D-Ge systems may enact a substantial improvement in the coherence properties of the charge degree of freedom. This could enable a more clear study of the ultrastrong-coupling physics in the $\eta \to 1$ limit and the potential to extend the coherence for a DQD charge or spin qubit in the $\eta \to 0$ limit even further.

Understanding and improving the coherence and control of the electron and hole charge degree of freedom in semiconductor systems is of paramount importance also for

future spin qubit applications, especially for systems where the spin is strongly hybridized with the orbital degree via a large real [44] or artificial spin-orbit field [45], enabling coupling with microwave photons. We anticipate that these findings will be of great significance for state-of-the-art charge and/or spin qubits as well as any hybrid QD-cavity designs, which are currently all limited by electrical noise.

ACKNOWLEDGMENTS

We acknowledge Christian Andersen, Mihai Gabureac, Theo Walter, and Johannes Heinsoo for the useful discussion and thank Christina Reissel for proofreading the manuscript. This work was supported by the Swiss National Science Foundation through the National Center of Competence in Research (NCCR) Quantum Science and Technology, the project Elements for Quantum Information Processing with Semiconductor/Superconductor Hybrids (EQUIPS), and ETH Zurich.

APPENDIX A: EXPERIMENTAL DETERMINATION OF THE DIPOLE STRENGTH η

In the following, we describe how the dipole strength η and the set of capacitance parameters $C_{\mathrm{LSG},1}$, $C_{\mathrm{RSG},1}$, $C_{\Sigma,1}$, $C_{\mathrm{LSG},2}$, $C_{\mathrm{RSG},2}$, $C_{\Sigma,2}$, and C_m are determined from the DQD charge stability diagram. Here, $C_{\mathrm{LSG},i}$ [$C_{\mathrm{RSG},i}$] is the capacitance between the left [right] side plunger gate and the ith dot, and $C_{\Sigma,i}$ is the total capacitance of the ith dot. C_m describes the interdot mutual capacitance. Together with the tunneling amplitude Δ, these parameters completely characterize the DQD system in our simplified model. A summary of the extracted parameters for the 11 studied DQD configurations is given in Table I. Some of these parameters are also plotted in Fig. 6. We cannot measure the capacitances between the resonator gate and the QDs (the resonator gate lever arm), since the gate is galvanically connected to ground via the resonator and, thus, cannot be dc biased.

The voltages applied to the T and CG gates [see Fig. 1(e)] are changed over hundreds of millivolts in order to realize the change of C_m/C_Σ necessary to explore the different η reported. Typically, smaller changes of a few millivolts are applied to fine-tune the interdot tunneling rate Δ/h by a few gigahertz, in order to realize the resonant condition with the resonator.

Dashed lines in the charge stability diagram [4] in Fig. 7 represent the plunger gate voltage differences between two consecutive sets of triple points for which the only difference is that the effective charge of one dot changes by one electron charge e, while the total electrostatic energy remains constant. Hence, one finds the four equations

$$\begin{pmatrix} C_{\mathrm{LSG},1} \\ C_{\mathrm{RSG},1} \\ C_{\mathrm{LSG},2} \\ C_{\mathrm{RSG},2} \end{pmatrix} = \begin{pmatrix} \Delta V_{L,1} & -\Delta V_{R,1} & 0 & 0 \\ 0 & 0 & \Delta V_{L,1} & -\Delta V_{R,1} \\ -\Delta V_{L,2} & \Delta V_{R,2} & 0 & 0 \\ 0 & 0 & -\Delta V_{L,2} & \Delta V_{R,2} \end{pmatrix}^{-1} \cdot \begin{pmatrix} e \\ 0 \\ 0 \\ e \end{pmatrix}, \tag{A1}$$

where the voltage differences $\Delta V_{L,1}$, $\Delta V_{R,1}$, $\Delta V_{L,2}$, and $\Delta V_{R,2}$ are given by the length of the dashed lines in Fig. 7. The charging energy, which is given by Eq. (2) in the main text, can be rewritten as

$$E_{n_1,n_2}(n_{G,i}) = E_{C,1}(n_1 - n_{G,1})^2 + E_{C,2}(n_2 - n_{G,2})^2 + E_{C,m}(n_1 - n_{G,1})(n_2 - n_{G,2}), \tag{A2}$$

TABLE I. Extracted parameters for the 11 DQD configurations presented in Fig. 4 in Sec. III in the main text.

Index	$C_{\Sigma,1}$ (fF)	$C_{\Sigma,2}$ (fF)	C_m (fF)	η	$g/2\pi$ (MHz)	$\Gamma_2/2\pi$ (MHz)	σ_ϵ (μeV)	Δ/h (MHz)	$\omega_r/2\pi$ (MHz)
1	0.561 ± 0.034	0.634 ± 0.071	0.488 ± 0.041	0.101 ± 0.064	41.63 ± 0.06	4.5 ± 0.2	0.171 ± 0.006	5420.8 ± 0.2	5437.0 ± 0.1
2	0.433 ± 0.037	0.474 ± 0.061	0.358 ± 0.041	0.117 ± 0.088	54.9 ± 0.1	4.8 ± 0.2	0.113 ± 0.009	5568.6 ± 0.3	5575.6 ± 0.14
3	0.599 ± 0.056	0.565 ± 0.034	0.473 ± 0.038	0.103 ± 0.065	48.8 ± 0.2	4.5 ± 0.2	0.107 ± 0.007	5435.1 ± 0.5	5578.6 ± 0.11
4	0.554 ± 0.068	0.41 ± 0.075	0.364 ± 0.060	0.204 ± 0.105	75.7 ± 0.2	5.5 ± 0.2	0.250 ± 0.008	5137.4 ± 0.4	5117.6 ± 0.14
5	0.656 ± 0.065	0.70 ± 0.053	0.506 ± 0.052	0.123 ± 0.079	56.4 ± 0.5	6.7 ± 0.2	…	5482 ± 3	5578.4 ± 0.4
6	0.611 ± 0.053	0.54 ± 0.058	0.443 ± 0.046	0.168 ± 0.071	86.3 ± 0.2	7.2 ± 0.2	0.120 ± 0.007	5633.5 ± 0.4	5649.0 ± 0.2
7	0.265 ± 0.045	0.31 ± 0.051	0.191 ± 0.034	0.184 ± 0.092	87.2 ± 0.4	6.5 ± 0.8	0.34 ± 0.007	5276 ± 1	5283.7 ± 0.6
8	0.333 ± 0.031	0.27 ± 0.041	0.250 ± 0.026	0.172 ± 0.078	111.1 ± 0.3	9.6 ± 0.3	0.273 ± 0.005	5145 ± 1	5180.3 ± 0.2
9	0.136 ± 0.045	0.32 ± 0.037	0.058 ± 0.017	0.419 ± 0.073	153.6 ± 1.9	28.3 ± 1.2	0.42 ± 0.02	4453 ± 4	4440.9 ± 0.3
10	0.330 ± 0.050	0.20 ± 0.023	0.048 ± 0.007	0.709 ± 0.031	260.5 ± 3.5	36.8 ± 0.9	…	4772.7 ± 9	4745.5 ± 0.9
11	0.412 ± 0.029	0.20 ± 0.050	0.257 ± 0.029	0.273 ± 0.076	65.9 ± 0.7	8.5 ± 1.1	0.328 ± 0.005	4243 ± 2	4271.6 ± 0.2

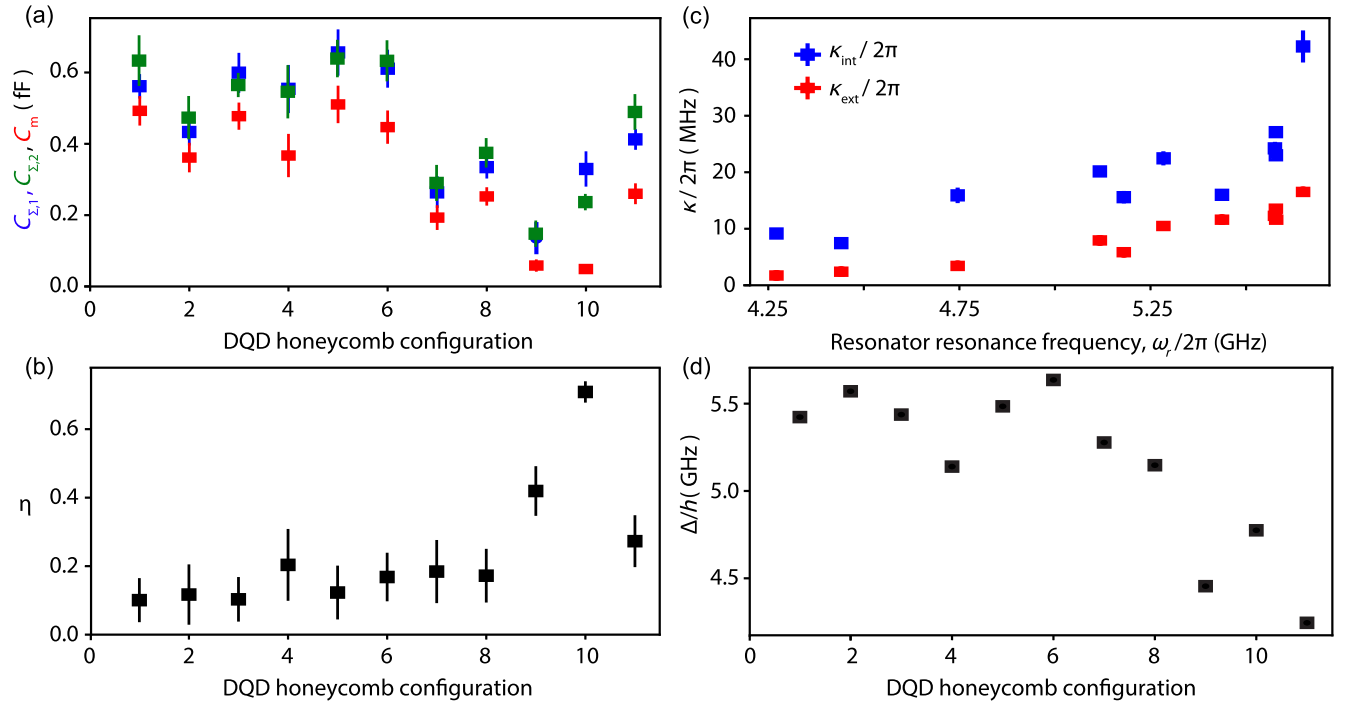

FIG. 6. Parameter comparison between the 11 configurations analyzed in the main text. (a) DQD capacitances $C_{\Sigma,1}$, $C_{\Sigma,2}$, and C_m. (b) Dipole strength η. (c) κ_{ext} and κ_{int}, extracted by fitting the reflectance of the bare SQUID array to a Lorentzian with the DQD deep in Coulomb blockade. (d) Interdot tunneling rates Δ/h obtained from the JC model [see dashed lines in Figs. 3(a)–3(c)]. In (c), the data are ordered according to the resonator frequency. In the remaining panels, the x axis is the configuration index.

where n_i is the number of electrons in dot i. Here, we introduce $n_{G,i}$, representing the effective number of electrons induced on dot i by the voltages on the gates. In our experiment, a voltage change on the left (right) side gate, denoted by ΔV^L (ΔV^R), results in a change $\Delta n_{G,1}$ ($\Delta n_{G,2}$) of $n_{G,1}$ ($n_{G,2}$) according to

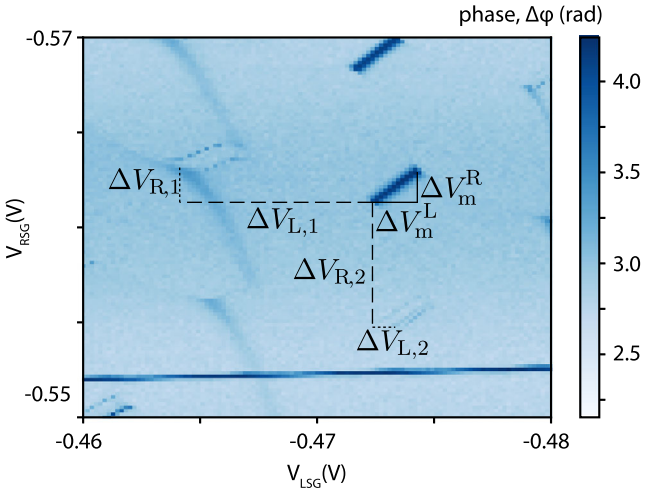

FIG. 7. An example of a DQD charge stability diagram. It shows the phase response of the resonator reflectance while changing the voltage of gates RSG and LSG [see Fig. 1(e)]. The six voltage differences indicated allow one to extract the QDs capacitances and the dipole strength η.

$$\begin{pmatrix} \Delta n_{G,1} \\ \Delta n_{G,2} \end{pmatrix} = \frac{1}{e} \begin{pmatrix} C_{\text{LSG},1} & C_{\text{RSG},1} \\ C_{\text{LSG},2} & C_{\text{RSG},2} \end{pmatrix} \cdot \begin{pmatrix} \Delta V^L \\ \Delta V^R \end{pmatrix}, \quad \text{(A3)}$$

and the charging energy matrix is represented by

$$\begin{pmatrix} E_{C,1} & E_{C,m}/2 \\ E_{C,m}/2 & E_{C,2} \end{pmatrix} = \frac{e^2}{2} \begin{pmatrix} C_{\Sigma,1} & -C_m \\ -C_m & C_{\Sigma,2} \end{pmatrix}^{-1}. \quad \text{(A4)}$$

Now we consider the solid black lines in Fig. 7 that connect adjacent triple points which are split due to the mutual interdot capacitance C_m. In the following, we use them to extract C_m, $C_{\Sigma,1}$, and $C_{\Sigma,2}$. Without losing generality, we consider the triple point at the intersects of the $\{(0,0),(0,1),(1,0)\}$ charge stability regions. The electrostatic energy at these triple point is given by

$$E_{0,0}(n_{G,i}^{(1)}) = E_{0,1}(n_{G,i}^{(1)}) = E_{1,0}(n_{G,i}^{(1)}). \quad \text{(A5)}$$

Similarly, the charging energy at the adjacent triple point corresponding to the intersect of the $\{(1,1),(0,1),(1,0)\}$ charge stability regions is given by

$$E_{1,1}(n_{G,i}^{(2)}) = E_{0,1}(n_{G,i}^{(2)}) = E_{1,0}(n_{G,i}^{(2)}). \quad \text{(A6)}$$

The voltage differences between these two triple points are denoted by ΔV_m^L and ΔV_m^R (lengths of solid black lines in Fig. 7). Plugging these voltage differences into Eq. (A3) as $\Delta V^L = \Delta V_m^L$ and $\Delta V^R = \Delta V_m^R$, we calculate the difference

of the effective electron numbers induced by the gates $\Delta n_{G,1}^{(m)}$ and $\Delta n_{G,2}^{(m)}$ between the two triple points. In order to calculate the three parameters C_m, $C_{\Sigma,1}$, and $C_{\Sigma,2}$, additionally to Eqs. (A5) and (A6), we consider the following relation which allows one to calibrate the energy scale in the DQD stability diagram:

$$\epsilon = E_{1,0} - E_{0,1} \tag{A7}$$

at a specific set of gate voltages. We measure ϵ by two-tone spectroscopy of the charge qubit at one specific gate voltage configuration and label the difference in the voltage on the left (right) gate between this configuration and the zero-detuning configuration by ΔV_ϵ^L (ΔV_ϵ^R). By plugging these voltage differences into Eq. (A3) as $V^L = \Delta V_\epsilon^L$ and $V^R = \Delta V_\epsilon^R$, we again convert the voltage differences into differences in the effective number of electrons induced by the gates which we call $\Delta n_{G,1}^{(\epsilon)}$ and $\Delta n_{G,2}^{(\epsilon)}$. Here, the superscript (ϵ) highlights the correspondence to one specific set of ϵ, ΔV_ϵ^L, and ΔV_ϵ^R.

Combining Eqs. (A2), (A5), (A6), and (A7), we find the charging energies as

$$\begin{pmatrix} E_{C,1} \\ E_{C,2} \\ E_{C,m} \end{pmatrix} = \begin{pmatrix} \Delta n_{G,1}^{(m)} & 0 & (\Delta n_{G,2}^{(m)} - 1)/2 \\ 0 & \Delta n_{G,2}^{(m)} & (\Delta n_{G,1}^{(m)} - 1)/2 \\ -2\Delta n_{G,1}^{(\epsilon)} & 2\Delta n_{G,2}^{(\delta)} & \Delta n_{G,1}^{(\epsilon)} - \Delta n_{G,2}^{(\epsilon)} \end{pmatrix}^{-1} \cdot \begin{pmatrix} 0 \\ 0 \\ \epsilon \end{pmatrix}. \tag{A8}$$

From the charging energies, the capacitances $C_{\Sigma,1}$, $C_{\Sigma,2}$, and C_m can be deduced from Eq. (A4). Finally, using Eq. (5) from the main text, we find the dipole strength as the main result of this appendix:

$$\eta = \frac{1 - 2C_m/(C_{\Sigma,1} + C_{\Sigma,2})}{1 + 2C_m/(C_{\Sigma,1} + C_{\Sigma,2})}, \tag{A9}$$

where the capacitance parameters are given as

$$C_m = \frac{e^2(\Delta V_\epsilon^L \Delta V_m^R + \Delta V_m^L \Delta V_\epsilon^R)}{\epsilon(\Delta V_{L,1}\Delta V_{R,2} - \Delta V_{L,2}\Delta V_{R,1})}, \tag{A10}$$

$$C_{\Sigma,1} = \frac{e^2(\Delta V_\epsilon^L \Delta V_m^R + \Delta V_m^L \Delta V_\epsilon^R)(\Delta V_{L,1}\Delta V_{R,2} - \Delta V_m^L \Delta V_{R,2} - \Delta V_{L,2}\Delta V_m^R - \Delta V_{L,2}\Delta V_{R,1})}{\epsilon(\Delta V_m^L \Delta V_{R,1} + \Delta V_{L,1}\Delta V_m^R)(\Delta V_{L,1}\Delta V_{R,2} - \Delta V_{L,2}\Delta V_{R,1})}, \tag{A11}$$

$$C_{\Sigma,2} = \frac{e^2(\Delta V_\epsilon^L \Delta V_m^R + \Delta V_m^L \Delta V_\epsilon^R)(\Delta V_{L,1}\Delta V_{R,2} - \Delta V_m^L \Delta V_{R,1} - \Delta V_{L,1}\Delta V_m^R - \Delta V_{L,2}\Delta V_{R,1})}{\epsilon(\Delta V_m^L \Delta V_{R,2} + \Delta V_{L,2}\Delta V_m^R)(\Delta V_{L,1}\Delta V_{R,2} - \Delta V_{L,2}\Delta V_{R,1})}. \tag{A12}$$

Note that when calculating $C_m/C_{\Sigma,i}$ the term $(\Delta V_\epsilon^L \Delta V_m^R + \Delta V_m^L \Delta V_\epsilon^R)/\epsilon$ cancels. Hence, $C_m/C_{\Sigma,i}$ and η can be determined directly from the charge stability diagram without considering the energy calibration step.

In the simplified case of identical dots, $C_{\Sigma,1} = C_{\Sigma,2} = C_\Sigma$, with a symmetric coupling to their respective gates, $C_{\mathrm{LSG},1} = C_{\mathrm{RSG},2}$, and neglecting cross-gate capacitances, $C_{\mathrm{RSG},1} = C_{\mathrm{LSG},2} = 0$, the expressions further simplify to

$$\frac{C_m}{C_\Sigma} = \frac{\Delta V_m}{\Delta V_g - \Delta V_m}, \tag{A13}$$

$$\eta = 1 - \frac{2\Delta V_m}{\Delta V_g}, \tag{A14}$$

where $\Delta V_m/\sqrt{2} \equiv \Delta V_m^L = \Delta V_m^R$ and $\Delta V_g/\sqrt{2} \equiv \Delta V_{L,1} = \Delta V_{R,2}$.

The error bars assigned to the extracted capacitances and to η are determined by attributing, in the above procedure, an uncertainty to the positions of the four triple points in the stability diagram (see Fig. 7). The errors are then propagated to the final results in Eqs. (A9)–(A12) using Gaussian error propagation.

In the following, Table I reports a summary of the extracted DQD capacitances, coupling, and DQD coherence parameters for the eleven DQD configurations presented in Fig. 4 in Sec. II of the main text. Instead, in Table II, we report the DQD gate voltages for the eleven configurations investigated in Sec. II of the main text.

TABLE II. The DQD gate voltages for the 11 configurations investigated in Sec. III in the main text.

Index	V_{CG} (mV)	V_T (mV)	V_{LSG} (mV)	V_{RSG} (mV)
1	−823.00	−623.00	−881.32	−946.48
2	−823.00	−623.00	−883.236	−937.35
3	−823.00	−727.00	−884.445	−789.79
4	−823.00	−818.00	−691.47	−751.60
5	−847.00	−847.00	−671.525	−641.20
6	−882.00	−882.00	−602.14	−648.68
7	−936.00	−936.00	−795.71	−593.76
8	−982.00	−982.00	−576.544	−613.92
9	−1040.00	−1040.00	−473.037	−562.02
10	−1050.00	−1050.00	−496.28	−574.92
11	−1030.00	−1030.00	−525.56	−494.35

APPENDIX B: CONSIDERATIONS ABOUT THE DEFINITION OF THE DIPOLE STRENGTH η IN EQ. (8)

Here, we report some further considerations about the definition of the dipole strength for a DQD, introduced in Eq. (8). First of all, η is dimensionless and independent on scales, such as the dot size or material constants. Second, since $C_\Sigma \geq C_m \geq 0$, its value ranges between zero and one. Third, we notice that zero mutual capacitance $C_m/C_\Sigma \to 0$ gives no suppression, $\eta \to 1$, and maximal mutual coupling $C_m/C_\Sigma \to 1$ gives perfect suppression, $\eta \to 0$. Here, it is useful to point out two possible limiting scenarios of increasing the interdot coupling to $C_m/C_\Sigma \to 1$. Among other options, one can take this limit with either C_Σ or $C_{\rm out}$ fixed. In the former, the numerator in Eq. (8) is decreasing, reflecting the sum rule in Eq. (6). The numerator is constant in the latter, and its only role is to render the dipole strength dimensionless and normalized to one. Finally, and what we deem most important, the definition of η as given in Eq. (8) is practical: The quantities defining η can be directly read off the standard charging diagram of the double dot, as illustrated in Figs. 2 and 7.

For illustration, we make the analogy with the typical microscopic model used to describe the origin of the coupling of the DQD electrical dipole moment $e \times d$ to the electrical field $\mathcal{E}$ generated by the resonator. In this case, we can write the coupling term as

$$\hbar g = \eta \times \hbar g_0 \equiv \eta \times e \times d \times \mathcal{E}, \tag{B1}$$

where we identify the *bare* dipole energy of the DQD and resonator as $\hbar g_0 = ed\mathcal{E} = 2e\sqrt{(\hbar\omega_r/2C_r)}[C_{G,1} - C_{G,2}/C_{\rm out}]$, defined through bare quantities e, d, and $\mathcal{E}$. Thus, Eq. (B1) expresses the coupling strength as the dipole energy arising from displacement of an electron by distance d in the electric field $\mathcal{E}$, modified by the dipole strength $\eta \in \langle 0, 1\rangle$. Such a definition anticipates the three different possible microscopic origins of the dipole strength for the dipolar interaction: The dot background (core) electrons can partially screen the electric field acting on the hopping (valence) electron ($\eta \times \mathcal{E}$); screening effects can reduce the effective hopping charge ($\eta \times e$); electrostatic tuning of the system may result in a configuration with reduced effective interdot distance ($\eta \times d$). Experimentally, we cannot distinguish these scenarios. We refer to them collectively as *renormalization of the dipolar coupling energy*. Equation (10) defines the dipole coupling g using more accessible parameters.

APPENDIX C: DETUNING SENSITIVITY TO CHARGE AND VOLTAGE FLUCTUATIONS

This appendix shows how the DQD detuning energy responds to a change in the electrostatic environment in correspondence with voltage or charge fluctuations of a nearby impurity. Our goal is to shed light on Eq. (5), especially in the case where the two dots have nonequal capacitance contributions. The first line in Eq. (5) can be cast into

$$\delta\epsilon = e\delta V_G \frac{C_G[d_\Sigma C_\Sigma + d_G(C_\Sigma - C_m)]}{C_\Sigma^2(1 - d_\Sigma^2/4) - C_m^2}. \tag{C1}$$

We introduce $C_G = (C_{G,1} + C_{G,2})/2$ and $C_\Sigma = (C_{\Sigma,1} + C_{\Sigma,2})/2$ for the average capacitances and $d_G = (C_{G,1} - C_{G,2})/C_G$ and $d_\Sigma = (C_{\Sigma,1} - C_{\Sigma,2})/C_\Sigma$ for fractional differences. The formula further simplifies upon introducing "polarizations" of the dot capacitances to the gate and to the outside of the DQD: $C_{{\rm out},d} = C_{\Sigma,d} - C_m$. Namely, we define the polarizations

$$P_G = \frac{C_{G,1} - C_{G,2}}{C_{G,1} + C_{G,2}}, \qquad P_{\rm out} = \frac{C_{\rm out,1} - C_{\rm out,2}}{C_{\rm out,2} + C_{\rm out,2}}. \tag{C2}$$

They relate to the fractional differences by $P_G = d_G/2$ and $P_{\rm out} = d_\Sigma C_\Sigma/2(C_\Sigma - C_m)$, and they take values between -1 and 1. $P_G \approx 1$ corresponds to the magnitude of the left dot capacitance to the gate V_G being much larger than that of the right dot and analogously for $P_{\rm out}$. Since we aim at the leading-order result, we neglect the $d_\Sigma^2/4$ term in the denominator of Eq. (C1), being higher order in the difference of the two total capacitances. With that, and using the polarizations, the detuning change is

$$\delta\epsilon = e\delta V_G \frac{C_{G,1} + C_{G,2}}{C_\Sigma + C_m}(P_G + P_{\rm out}), \tag{C3}$$

which is a generalization of the second line in Eq. (5): The difference of the two dots gives rise to an additional polarization, $P_{\rm out}$. Using Eq. (C3) instead of Eq. (C1), the expression in Eq. (7) reads

$$\delta\epsilon = eV_G \frac{C_{G,1} + C_{G,2}}{C_{\rm out}}(P_G + P_{\rm out})\eta, \tag{C4}$$

where $C_{\rm out} = C_\Sigma - C_m$ and the last term is the dipole strength as given in Eq. (8). In other words, our definition of η remains the same even if the dots are not equal.

We now derive the detuning change with respect to a charge impurity fluctuation. Concerning the electrostatic description, a charge impurity is an object similar to a dot: Its primary variable is the charge, and the voltage is a derived variable. Postponing the derivation and discussion of a model containing charge impurities to a separate publication, we state here only the result; the analog of Eq. (C1) with changing impurity i charge by δQ_i is

$$\delta\epsilon = e\frac{\delta Q_i}{C_{\Sigma,i}}\frac{C_{i,1}+C_{i,2}}{C_\Sigma + C_m}(P_i + P_{\text{out}}), \tag{C5}$$

where $C_{i,d}$ is the capacitance between the impurity i and the dot d, the polarization of these capacitances is $P_i = (C_{i,1} - C_{i,2})/(C_{i,1} + C_{i,2})$, and $C_{\Sigma,i}$ is the impurity self-capacitance. We conclude that there is a complete analogy between Eqs. (C3) and (C5) upon interpreting $\delta Q_i/C_{\Sigma,i}$ as the equivalent voltage fluctuation.

APPENDIX D: HOW DO FIGURES OF MERIT SCALE WITH THE DIPOLE STRENGTH

Here, we discuss how the most important circuit-QED figures of merit scale with the dipole strength η. The scaling depends on whether the noise spectrum is singular (diverges at zero frequency) or regular and whether it couples to the qubit energy linearly or quadratically. Using the results of Ref. [28] and Eqs. (1), (7), and (8), we obtain Tables III and IV. In the former, one can see that in any scenario both decoherence and relaxation increase with increasing η. We find two possible power laws, linear and quadratic. The decoherence rate is linear in η if the noise is singular, such as a $1/f$ noise, and couples to the qubit linearly, provided that the qubit is not at a sweet spot. We observe linear scaling of the decoherence in our experiments. In all other considered scenarios, the decoherence should be quadratic in η and the relaxation rate should always be quadratic in η. Aiming at maximal coherence calls for minimizing η, which is the motivation for the first set of experiments described in Sec. III. Turning to Table III, the first line gives a qubit-resonator coupling proportional to η. Maximizing the coupling, as in aiming at the ultrastrong-coupling regime, requires one to maximize η. Experimentally, this is realized in the experiments outlined in Sec. IV.

We now comment on two additional figures of merit, the quality factor and cooperativity. They contain the coherence time, which we take as the inverse of the decoherence rate given in Table III. We assume that the scaling of the decoherence and the relaxation is the same (quadratic) or that the relaxation can be made negligible if they differ. Under this assumption, the quality factor might benefit from decreasing η, while the cooperativity from increasing it. Whether the benefit is realized depends on the character of the noise.

In conclusion, Table IV uncovers a surprisingly large number of scenarios: The chosen figure of merit, the noise character, whether the qubit can be robustly kept at a sweet spot, and whether the relaxation is dominating the decoherence all play a nontrivial role. Their combination decides whether maximization or minimization of η is to be strived for.

TABLE III. Qualitative dependence of the qubit decay rates on the qubit properties, including the dipole strength η. The "coupling" denotes the power with which the noise variable δV changes the qubit energy; for example, quadratic means $\delta\hbar\omega_q \propto \delta V^2$. "Singular" means that the noise diverges at zero frequency, for example, for $1/f$ noise. For quadratic coupling, the low-frequency and high-frequency parts of the noise spectrum are defined with respect to the inverse evolution time. "Resonant" stands for noise relevant only at the qubit frequency. "Decay type" denotes the functional form of the decay envelope, such as the one in Eq. (11) which happens to be Gaussian. Qubit "configuration" comprises the detuning and tunneling, and "sensitivity" denotes the derivative of the detuning with respect to the fluctuating voltage $\partial_V\epsilon \equiv \partial\epsilon/\partial V_G$, which can be obtained from Eq. (5). Finally, "suppression" denotes the scaling of Eq. (8). An example how to read this table: For a system dominated by a regular noise coupled linearly to the qubit, the qubit coherence decay is exponential, with a pure dephasing rate $\Gamma_\varphi \propto \Delta^2/(\epsilon^2+\Delta^2)(\partial_\nu\epsilon)^2\eta^2$.

				Dependence on qubit		
Decay process	Coupling	Noise	Decay type	Configuration	Sensitivity	Suppression
Pure dephasing	Linear	Singular	Gaussian	$\frac{\epsilon}{\sqrt{\epsilon^2+\Delta^2}}$	$\partial_V\epsilon$	η
	Linear	Regular	Exponential	$\frac{\Delta^2}{\epsilon^2+\Delta^2}$	$(\partial_V\epsilon)^2$	η^2
	Quadratic	Low-freq.	Algebraic	$\frac{\Delta^2}{(\epsilon^2+\Delta^2)^{3/2}}$	$(\partial_V\epsilon)^2$	η^2
	Quadratic	High-freq.	Exponential	$\frac{\Delta^2}{(\epsilon^2+\Delta^2)^{3/2}}$	$(\partial_V\epsilon)^2$	η^2
Relaxation	Linear	Resonant	Exponential	$\frac{\Delta^2}{\epsilon^2+\Delta^2}$	$(\partial_V\epsilon)^2$	η^2

TABLE IV. Scaling of several figures of merit with the dipole strength. As follows from Eq. (10), we use $g \propto \eta$ for the interaction strength and the results from Table III for the pure dephasing rate Γ_φ. Here, we work in the hypothesis that the decoherence is dominated by dephasing process ($\Gamma_2 \sim \Gamma_\phi$), which is a reasonable assumption for DQD charge qubits.

		Dominant noise	
Figure of merit	Formula	Linear-singular	Other
Coupling to cavity	g	η^1	
Coherence time	$T_2^* = 1/\Gamma_\varphi$	η^{-1}	η^{-2}
Quality factor	$Q = g/\Gamma_\varphi$	η^0	η^{-1}
Cooperativity	$g^2/\Gamma_\varphi\kappa$	η^1	η^0

APPENDIX E: SQUID AND JUNCTION ARRAY HIGH-IMPEDANCE RESONATORS

High-impedance resonators represent a valuable tool to increase the vacuum voltage fluctuations to maximize the coupling strength with the two-level electrical dipole moment. They allow one to reach the strong-coupling regime for electrons confined in semiconductor DQDs [10]. For superconducting artificial atoms electrically coupled to the microwave radiation, it has been recently demonstrated that high-impedance resonators enable reaching a much higher coupling strength, which brings the system in the ultrastrong and deep strong-coupling regimes [25,26].

The SQUID and JJ array resonators, represented in Fig. 8, are 1D Josephson-junction metamaterials with a multimode spectrum [36]. The choice of design parameters ensures that the array exhibits its fundamental mode within the measurement bandwidth and well separated in frequency from its second mode [36]. In Figs. 8(a) and 8(b) [8(c) and 8(e)], we report a micrograph of [a circuit model for] the SQUID and JJ array resonators, respectively. The base unit of the SQUID [JJ] array resonator is enclosed by the dashed red [blue] line in Figs. 8(a), 8(c), and 8(d) [8(b), 8(e), and 8(f)]. The fabrication process of the SQUID array, based on the shadow evaporation technique, generates the two small Josephson junctions in parallel (the SQUID junctions, in red) that are in series with an extra larger junction (in blue), of approximately 11 times larger footprint, as we can see in Fig. 8(a).

We realize SQUID junctions with inductance $L_S \sim 1.25$ nH and capacitance $C_S \sim 80$ fF, while the large junctions have $L_J^\star \sim 0.11$ nH and $C_J^\star \sim 880$ fF. Each section of the SQUID array contributes on average a stray capacitance to ground of $C_0 \sim C_{\mathrm{gnd}}/N = C_0^J + C_0^S$ (see Table V), where $C_0^J \sim 6C_0^S$ is the average capacitance to ground of the series junction. Therefore, the part of the base unit containing the extra junction dominates the stray

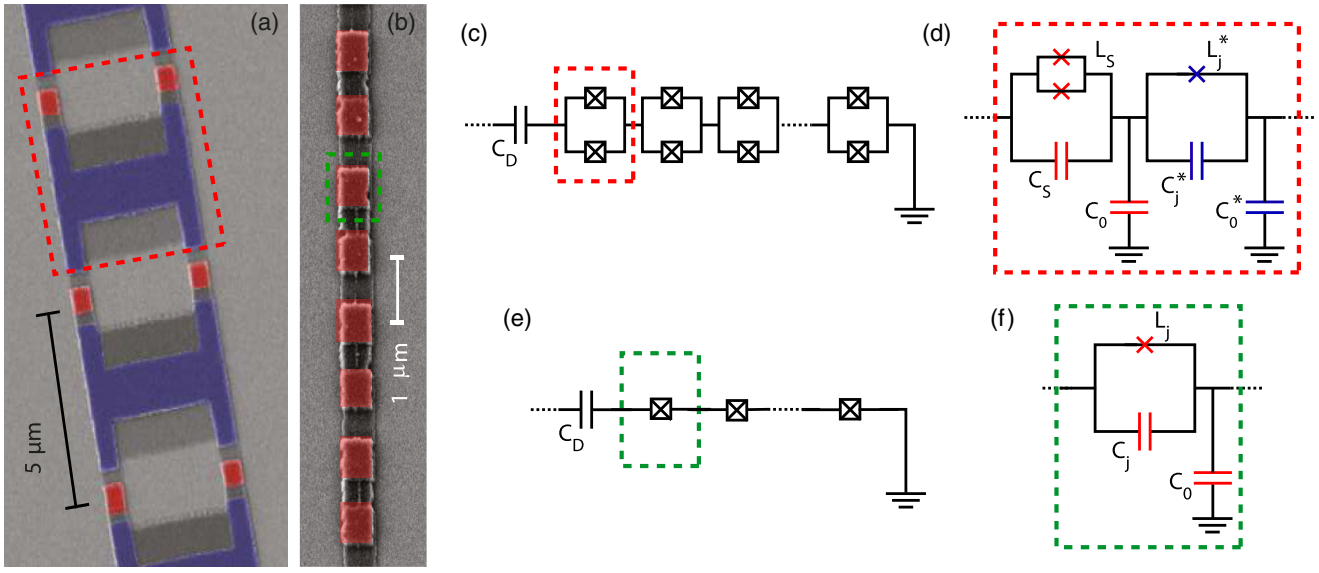

FIG. 8. Comparison between a SQUID and a junction array resonator. (a) False-colored SEM micrograph of a section of a SQUID array. The dashed red line encloses the unit cell of the SQUID array. (b) False-colored SEM micrograph of a section of a Josephson-junction array. The dashed green line encloses the unit cell of the array, with a single 0.5×0.9 μm^2 Josephson junction. (c) Schematic circuit for a $\lambda/4$ SQUID array resonator. $C_D = C_c + C_{\mathrm{RPG}} + C_g$ represents the capacitive coupling between the resonator array and the microwave feedline, the DQD device, and the rest of the DQD gates. The other end of the array is grounded. (d) Circuit schematic of the unit cell of the SQUID array. L_S and $L_J^\star$ represent the inductance of each SQUID junction (red) and of the extra Josephson junction (blue) connected in series, while C_S (red) and $C_J^\star$ (blue) represent their junction capacitance. C_0 and $C_0^\star$ are their respective capacitances to the ground. (e) Schematic circuit for a $\lambda/4$ JJ array. (f) Circuit schematic of the JJ array's unit cell. L_J represents the Josephson inductance, while C_J and C_0 are the junction capacitance and the stray capacitance to ground, respectively.

TABLE V. Comparison between SQUID and JJ array resonators.

	SQUID array	Junction array
Z_r (kΩ)	1.1	3.8
$\omega_r/2\pi$ (GHz)	6.2 (tunable)	5.665
$\kappa_{\rm int}/2\pi$ (MHz)	Fig. 6(c)	23.0
$\kappa_{\rm ext}/2\pi$ (MHz)	Fig. 6(c)	4.0
N	34	72
$\omega_p/2\pi$ (GHz)	16.6	16.1
Length (μm)	200	70
K_{00} (kHz)	5	60
$L_{\rm tot}$ (nH)	31	102
$C_{\rm gnd}$ (fF)	19	5
C_c (fF)	2.5	1.5
C_g (fF)	1.5	1.5

capacitance to the ground per section but adds a negligible contribution to the total array inductance. This limits the impedance of the resonator array's fundamental mode.

We model the arrays as distributed $\lambda/4$ resonators, being shunted to ground on one end [see Figs. 1(c) and 1(d)]. The capacitances between the array resonator and the right QD, the microwave feedline, and the rest of the DQD depletion gates are estimated to be $C_{\rm RPG} \sim 0.07$ fF, $C_c \sim 3$ fF, and $C_g \sim 1.5$ fF, respectively.

As shown in Fig. 8(f) and reported in Table V, we model each unit cell of the JJ array with a parallel circuit of an inductance $L_J \sim 1.5$ nH and a capacitance $C_J \sim 40$ fF, connected in series with a capacitance $C_0^{\rm JJ}$ to ground. For $N = 70$ junctions in series, we obtain a total array resonator length of about 70 μm, with an estimated total array inductance of $L_{\rm tot} \sim 102$ nH and a total stray capacitance to ground of $C_{\rm gnd} \sim 4.9$ fF. This allows us to estimate a JJ array resonator impedance $Z_r^{\rm JJ} \sim \sqrt{L_{\rm tot}/(C_{\rm gnd}+C_c+C_g+C_{\rm RPG})} \sim 3.8\,{\rm k\Omega}$, which is almost 4 times higher than the SQUID array impedance and allows one to increase the coupling strength with the DQD electric-dipole moment of a factor $\sqrt{Z_r^{\rm JJ}/Z_r^{\rm Sq}} \sim 2$.

APPENDIX F: MASTER EQUATION—DISSIPATIVE DYNAMICS OF DQD AND RESONATOR

Here, we give a short introduction to the theoretical modeling of the experimental data. The model includes the DQD, the resonator, and the microwave drive through a transition line. For simplicity, we use the convention $\hbar = 1$ in this section. The dissipative dynamics of the system are described by the master equation

$$\dot{\rho} = -i[H,\rho] + \sum_k \mathcal{L}_k \rho, \tag{F1}$$

where H is the Hamiltonian of the system and $\mathcal{L}_k\rho$ describe different dissipative channels introduced in the following.

1. Hamiltonian

The DQD is well described by the Hamiltonian

$$H_{\rm DQD} = \frac{1}{2}\epsilon\sigma_z + \frac{1}{2}\Delta\sigma_x = \frac{1}{2}\hbar\omega_q\tilde{\sigma}_z, \tag{F2}$$

with the Pauli matrices σ in the DQD position basis and $\tilde{\sigma}$ in its eigenbasis and where ϵ is the detuning and Δ is the tunnel splitting between the two dots. The DQD level splitting is $\hbar\omega_q = \sqrt{\epsilon^2+\Delta^2}$. The resonator is described by

$$H_{\rm res} = \hbar\omega_r a^\dagger a, \tag{F3}$$

with its resonance frequency ω_r and the bosonic annihilation operator a. The coupling between DQD and resonator corresponds to the quantum dot dipole moment and the electric field of the harmonic oscillator mode, so we write

$$\begin{aligned} H_{\rm DQD-res} &= \hbar g_0 \sigma_z (a + a^\dagger) \\ &= \hbar g_0 (\cos\varphi\tilde{\sigma}_z + \sin\varphi\tilde{\sigma}_x)(a + a^\dagger), \end{aligned} \tag{F4}$$

with the DQD mixing angle $\tan\varphi = (\epsilon/\Delta)$. The total system Hamiltonian is then

$$H = H_{\rm DQD} + H_{\rm res} + H_{\rm DQD-res}. \tag{F5}$$

2. Dissipative processes

The quantum dot and resonator are unavoidably coupled to the environment, leading to energy loss and dephasing. For the resonator, incoherent photon loss can be described in the master equation through a dissipative term

$$\mathcal{L}_{\rm res}\rho = \kappa_{\rm int}\mathcal{D}[a]\rho, \tag{F6}$$

with the internal photon loss rate $\kappa_{\rm int}$. In practice, the resonator decay consists of an internal component $\kappa_{\rm int}$, resulting from coupling to the intrinsic environment, and an external coupling rate $\kappa_{\rm ext}$, resulting from coupling to external modes, such as the transmission lines used for driving. Here, the external coupling is taken into account through the SLH cascading of an external driving field, described in the next section, so that we include only the intrinsic losses $\kappa_{\rm int}$. For the DQD, we assume a transversal decay channel, leading to energy relaxation at rate Γ_1, as well as a pure dephasing process due to fluctuations in the level splitting, leading to dephasing at rate $\Gamma_2 = \frac{1}{2}\Gamma_1 + \Gamma_\varphi$. The contributions to the master equation due to the dissipative dynamics of the DQD are then given by

$$\mathcal{L}_{\rm DQD}\rho = \Gamma_1\mathcal{D}[\tilde{\sigma}_-]\rho + \frac{1}{2}\Gamma_\varphi\mathcal{D}[\tilde{\sigma}_z]\rho. \tag{F7}$$

3. SLH model—Driven, dissipative dynamics of DQD and resonator

We use the SLH cascaded quantum systems approach to model scattering of microwave photons in the transmission line off the $\lambda/4$ resonator [40,46,47]. We cascade in a drive field for the resonator, which adds an effective drive term to the Hamiltonian as

$$H_{\mathrm{drive}} = \frac{1}{2i}\sqrt{\kappa_{\mathrm{ext}}}(\alpha a^{\dagger} - \alpha^{*} a), \tag{F8}$$

where we assume a single-sided, $\lambda/4$-type cavity driven with a coherent state of amplitude α. Here, we additionally transform the system into the rotating frame at the drive frequency ω_d of the coherent field input α. The cascading also adds another dissipative part to the master equation, which describes the decay of the resonator modes into the transmission line, which is assumed to have a constant spectrum. This term can be written as

$$\mathcal{L}_{\mathrm{SLH}}\rho = \mathcal{D}[\hat{L}]\rho \tag{F9}$$

with the decay operator

$$\hat{L} = \sqrt{\kappa_{\mathrm{ext}}}a + \alpha\mathbb{1}. \tag{F10}$$

Using this formalism, we can now calculate the amplitude β and photon flux n of the field scattered off the resonator as

$$\beta = \mathrm{Tr}\{\hat{L}\rho\}, \qquad n = \mathrm{Tr}\{\hat{L}^{\dagger}\hat{L}\rho\}, \tag{F11}$$

where ρ is the solution of the total master equation [Eq. (F1)], now also including the drive and decay term from the cascading procedure [Eqs. (F8) and (F9)]. As equilibration of the field in the transmission lines happens typically very fast, we can assume that scattering in experiments happens in the steady state of the system, so that we need only to calculate the steady-state density matrix $\bar{\rho}$ for all cases.

4. Visibility of vacuum Rabi splitting

In order to find analytical expressions for the scattered field in the special case where DQD and resonator are tuned to resonance, we take the analogy to the case of a two-level system embedded in a waveguide; cf. the supplemental material in Ref. [48]. For exact resonance between DQD and resonator, $\omega_r = \omega_q = \omega_0$, the eigenstates of the coupled system are $|\pm\rangle = \frac{1}{\sqrt{2}}(|0,e\rangle \pm |1,g\rangle)$. We are focusing on driving the transition between the total system ground state $|0,g\rangle$ and one of the coupled eigenstates $|\pm\rangle$, analogous to the two-level system case. We diagonalize the total Hamiltonian of the resonator plus the DQD and consider the relevant operators in the diagonal basis, when reduced to a subset of states, i.e., the total system ground state $|0,g\rangle$ and either of the two maximally mixed eigenstates $|\pm\rangle$. For each of these transitions, we write the input-output relations in the SLH formalism analogously to the case of a driven two-level system to find the reflectance of the $\lambda/4$-type resonator in resonance with the DQD. For small drive amplitudes α far from saturation, we find to lowest order in α

$$r_{\pm} = \beta/\alpha = 1 - \frac{2\kappa_{\mathrm{ext}}}{[\kappa_{\mathrm{ext}} + \kappa_{\mathrm{int}} + 2\Gamma_2 + 4i(\omega_0 - \omega_d \pm \frac{1}{2}g_0)]}, \tag{F12}$$

where ω_d is the frequency of the drive field and g_0 is the coupling strength between resonator and DQD. As we assume perfect resonance between DQD and resonator, the two expressions differ only in the position of the resonance. For resonant driving of either transition, i.e., when $\omega_d = \omega_0 \pm \frac{1}{2}g_0$, $r_{\pm}$ reduces to

$$\begin{aligned} r_{\pm,\mathrm{res}} &= 1 - |S_{11}| = 1 - \frac{2\kappa_{\mathrm{ext}}}{(\kappa_{\mathrm{ext}} + \kappa_{\mathrm{int}} + \Gamma_1 + 2\Gamma_{\varphi})} \\ &= 1 - \frac{\kappa_{\mathrm{ext}}}{2\Gamma_{2,\pm}}. \end{aligned} \tag{F13}$$

Thus, the depth of the reflection peak on resonance is given by the ratio of the external coupling of the resonator to twice the total linewidth of the DQD-resonator hybridized states, $\Gamma_{2,\pm} = \frac{1}{4}(\kappa_{\mathrm{ext}} + \kappa_{\mathrm{int}} + \Gamma_1 + 2\Gamma_{\varphi})$, analogous to the case of scattering off a two-level system [48]. A plot of the visibility of the Rabi modes, extracted according to Eq. (F13), is reported as a function of η in Fig. 4(f) in the main text and as a function of the renormalized coupling strength $\bar{g}_{\perp}$ in Fig. 9(b).

5. Fits

Peaks from experiments are fitted to the Hamiltonian level structure, i.e., the position of levels in Eq. (F5). When fitting the full transmission curve as a function of the frequency, the SLH model is used, where for simplicity we set $\gamma_1 = 0$, as only the total DQD linewidth is relevant for these fits.

APPENDIX G: SYSTEM COOPERATIVITY

A high-fidelity technology must exchange information with preserved coherence, i.e., demonstrate the so-called strong-coupling regime. This criterion, which must be met for any useful quantum application, is characterized by a coupling between two subsystems that is stronger than the mean of the losses in both of them. As such, it is useful to introduce the cooperativity $C = \bar{g}_{\perp}^2/[\Gamma_2(\kappa_{\mathrm{ext}} + \kappa_{\mathrm{int}})]$ to characterize the strength of a light-matter interaction in our hybrid system and to compare to what was already achieved for similar devices deployed in previous experiments [35]. The strong-coupling regime corresponds to a cooperativity which is greater than unity. Thus, the coupling is strong in the sense that at resonance nearly every photon entering the cavity is coherently transferred into the matter system.

In Fig. 9(a), we report the system cooperativity extracted for the 11 studied DQD configurations as a function of the

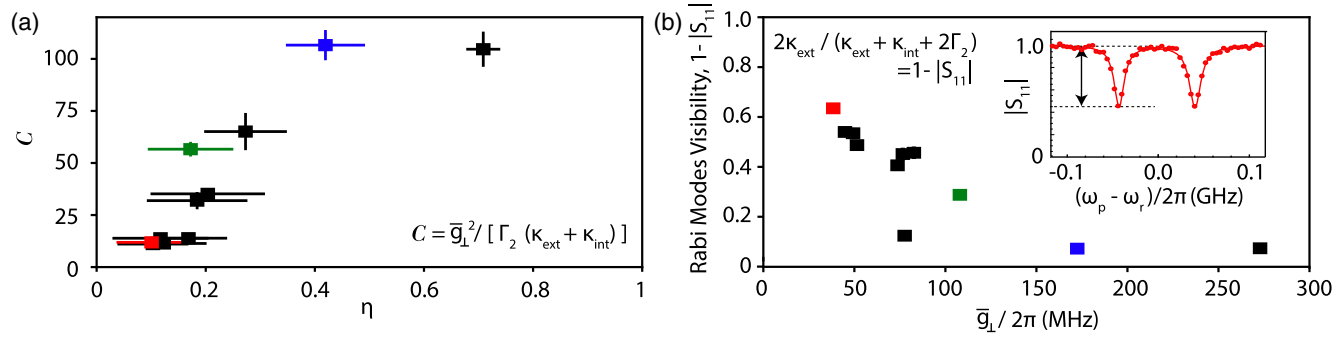

FIG. 9. Extracted figures of merit of light-matter hybridization. (a) System cooperativity $C = \bar{g}_\perp^2/[\Gamma_2(\kappa_{ext} + \kappa_{int})]$. (b) Visibility of the vacuum Rabi modes at resonance $(1 - |S_{11}|) = 2\kappa_{ext}/(\kappa_{ext} + \kappa_{int} + 2\Gamma_2)$ versus the DQD-SQUID array coupling strength $\bar{g}_\perp$.

dipole strength η. We notice how, despite increasing η increases the DQD decoherence rate Γ_2 (see Fig. 4), the cooperativity overall increases with η. This is in line with what is illustrated in the main part of the paper, where we report that $\bar{g}_\perp, \Gamma_2 \propto \eta$, and therefore $C \propto \eta$. Making use of the described tuning strategy for the DQD electric-dipole strength, we push the limits for the cooperativity achieved for the semiconductor QD-resonator hybrid device above 100, representing the current record of cooperativity for a QD-resonator hybrid system. Furthermore, by adequately filtering the DQD gate lines, it is shown that it is possible to keep a resonator linewidth < 1 MHz [49,50], which, if implemented in our device, could allow achieving a cooperativity of up to $C \sim 1500$.

APPENDIX H: RENORMALIZATION OF THE COUPLING STRENGTHS [EQ. (12)]

In the following, we describe the strategy used to renormalize the coupling strengths extracted from the 11 studied DQD configurations in Sec. III [see Eq. (12)]. Renormalization of the coupling strengths is necessary for comparison, because the hybridized spectra for the investigated DQD configurations are taken at not exactly the same resonator frequency and DQD tunneling amplitude (see Table I). The first term in Eq. (12), $\Delta/\hbar\omega_r$, originates from the mixing angle renormalization of the DQD dipole strength [6] [see Eq. (1)]. In Fig. 10(a), we report a study of the coupling strength between a DQD and a resonator as a function of the resonator frequency. The data originate from a similar device with a nominally identical DQD coupled to a SQUID array resonator. The data are acquired by spectroscopically measuring avoided crossings between the resonator and the DQD charge qubit while keeping the DQD at its sweet spot ($\epsilon = 0$). The resonance frequency of the DQD charge qubit is changed systematically by changing its interdot tunneling amplitude Δ via the voltages applied to the depletion gates, and the frequency tunability of the SQUID array allows one

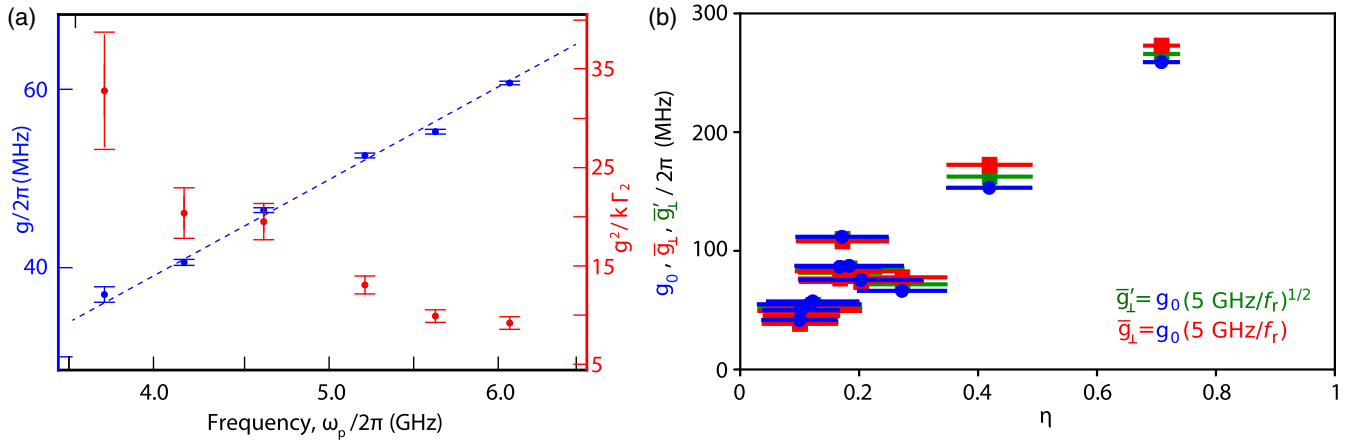

FIG. 10. (a) (Left axis) $g/2\pi$ extracted by measuring a Rabi mode splitting for the DQD qubit in resonance at $\epsilon = 0$ with the SQUID array fundamental mode, for different resonator frequency. (Right axis) system cooperativity $g^2/(\kappa\Gamma_2)$ at different resonator frequency. During these measurements, the DQD system is kept at the sweet spot $\epsilon = 0$. (b) Comparison of the extracted coupling strengths corrected only for the mixing angle $g_0 = g\Delta/\omega_r$ with normalized $\bar{g}_\perp \propto g_0[5\ \text{GHz}/(\omega_r/2\pi)]$ and $\bar{g}'_\perp \propto g_0\sqrt{[5\ \text{GHz}/(\omega_r/2\pi)]}$.

to bring the resonator into resonance with the charge qubit.

The extracted evolution of the coupling rate g as a function of the resonator frequency $\omega_r \sim \omega_q$ can be modeled accurately by a simple linear dependence [see the blue dotted line in Fig. 10(a)]. Instead, considering that $Z_r = 1/(\omega_r C_r)$, from Eq. (10), $g \propto \sqrt{Z_r}\omega_r \propto \sqrt{\omega_r}$ is expected assuming a simple lumped-element equivalent model of the resonator under the condition that the tuning process of the interdot tunneling rate appreciably modifies neither the DQD electrical dipole moment nor its capacitive coupling to the resonator gate (DQD lever arm). The linear scaling of g against ω_r suggests that other mechanisms take place in either the resonator impedance or the DQD electric-dipole moment during the tuning procedures of the interdot tunneling and SQUID array resonance. The change in tunnel rate or DQD shape could present a considerable influence on the magnitude of the electrical dipole moment of the DQD and, thereby, on the coupling strength. A complete understanding of these mechanisms requires further investigations.

Figure 10(b) shows a comparison of the extracted coupling strengths corrected for the mixing angle $g_0 = g\Delta/\hbar\omega_r$ and with the normalized $\bar{g}_\perp \propto g_0(5\ \mathrm{GHz}/\omega_r)$ and $\bar{g}'_\perp \propto g_0\sqrt{5\ \mathrm{GHz}/\omega_r}$. We notice that, in our dataset, the correction originating from the normalization choice does not exceed 10% of the bare extracted coupling rates.

APPENDIX I: ADDITIONAL DATA

Here, we report some additional measurements and datasets which the reader can find useful to better interpret the measurements reported in the main text.

Figure 11(a) reports a study of a DQD configuration, distinct from the one reported in Fig. 5 in the main text. This new configuration is obtained by *in situ* tuning the DQD dipole strength to $\eta \sim 0.5$. The red (blue) line in Fig. 11(b) represents a fit to the data obtained using the Rabi (JC) model from which we extract $g_R/2\pi = 350 \pm 3$ MHz ($g_{\mathrm{JC}}/2\pi = 351 \pm 2$ MHz). A fit of a master equation model [solid orange line in Fig. 11(c)] to the Rabi mode spectrum, obtained by changing the probe frequency along the DQD detuning value indicated by the black arrows in Fig. 11(b), yields a splitting of $g/2\pi \sim 373.4 \pm 0.3$ MHz, with a DQD charge decoherence of $\Gamma_2/2\pi \sim 56.3 \pm 0.2$ MHz. For this DQD electrostatic configuration, the system is in the strong-coupling regime ($g > \kappa/2 + \Gamma_2$) but comes with $g_{R,\mathrm{JC}}/\omega_r \sim 0.062$, which, despite being very high for a DQD-resonator hybrid device, does not promote the system in the USC regime. The Figs. 12(a), 12(b), and 12(c) show the SQUID-array resonator reflectance amplitude $|S_{11}|$ versus DQD detuning ϵ/h corresponding to Figs. 3(a), 3(b), and 3(c) but without the overlaid fitting curves. Similarly, the Figs. 13(a) and 13(b) show the junction array resonator reflectance amplitude $|S_{11}|$ versus DQD detuning ϵ/h corresponding to Figs. 5(b) and 11(b) without the overlaid fitting curves.

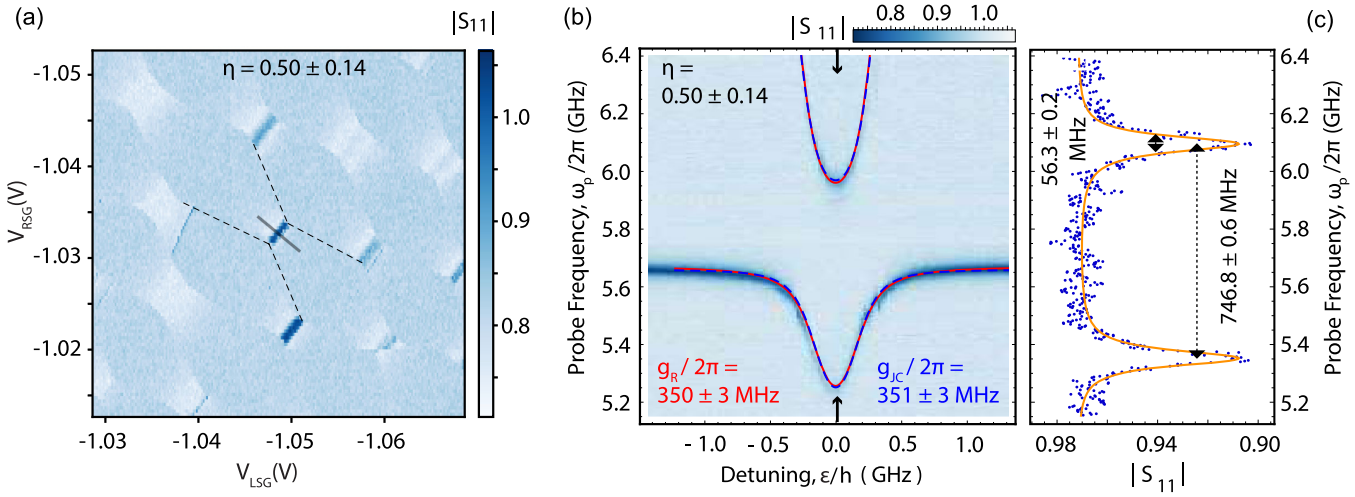

FIG. 11. Investigation of a configuration approaching the ultrastrong-coupling regime for a DQD with $\eta \sim 0.50 \pm 0.14$ coupled to a JJ array. (a) Charge stability diagram of the DQD measured by monitoring the change in resonator reflectance amplitude $|S_{11}|$ for the extracted dipole strength $\eta \sim 0.50 \pm 0.14$. (b) Resonator amplitude response $|S_{11}|$ taken by varying the DQD detuning ϵ along the gray line indicated in (a) by applying properly chosen voltages to the two side gates. The red (blue) lines are independent fits to the Rabi (JC) model (see Appendix F). (c) Line cut representing $|S_{11}|(\omega_p/2\pi)$ taken along the black arrows in (b). The orange line represents a fit to a JC master equation model. The resonator losses are $\kappa_{\mathrm{int}}/2\pi = 19.5$ MHz and $\kappa_{\mathrm{ext}}/2\pi = 4.3 \pm 0.1$ MHz.

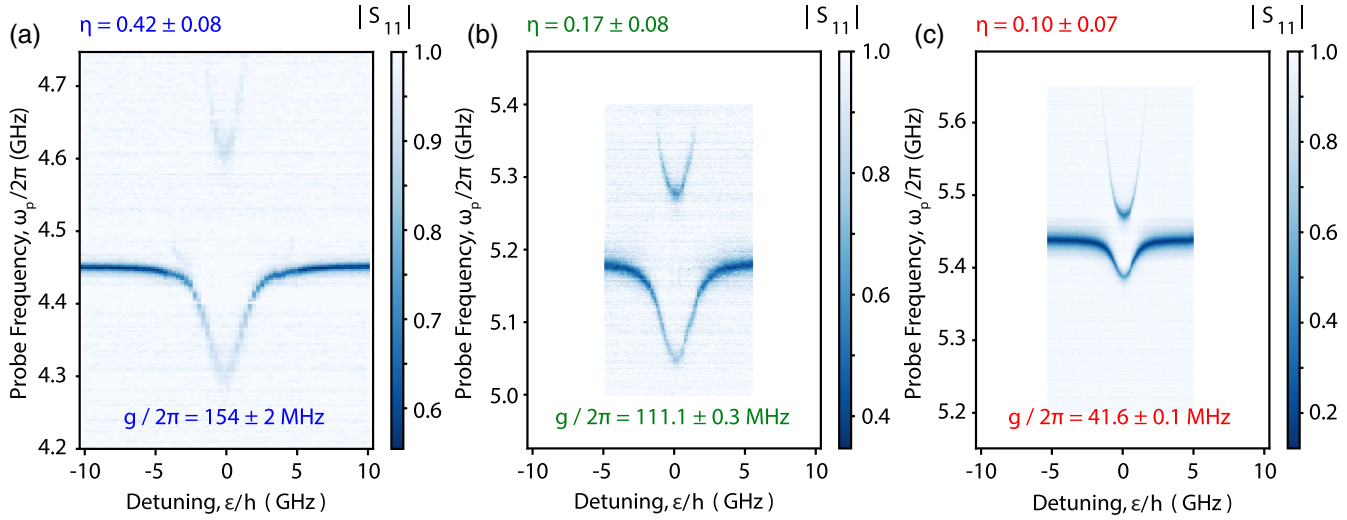

FIG. 12. Response of the SQUID array resonator reflectance amplitude $|S_{11}|$ versus DQD detuning ϵ in correspondence of three distinct dipole strengths (a) $\eta \sim 0.42 \pm 0.08$ (blue), (b) $\eta \sim 0.17 \pm 0.08$ (green), and (c) $\eta \sim 0.10 \pm 0.07$ (red) [the corresponding DQD charge stability diagrams are reported in Figs. 2(e), 2(d), and 2(c), respectively]. The three resonant spectrums are obtained by tuning the SQUID array in resonance with the DQD charge excitation frequency for $\epsilon = 0$. Data are already reported in Figs. 3(a)–3(c).

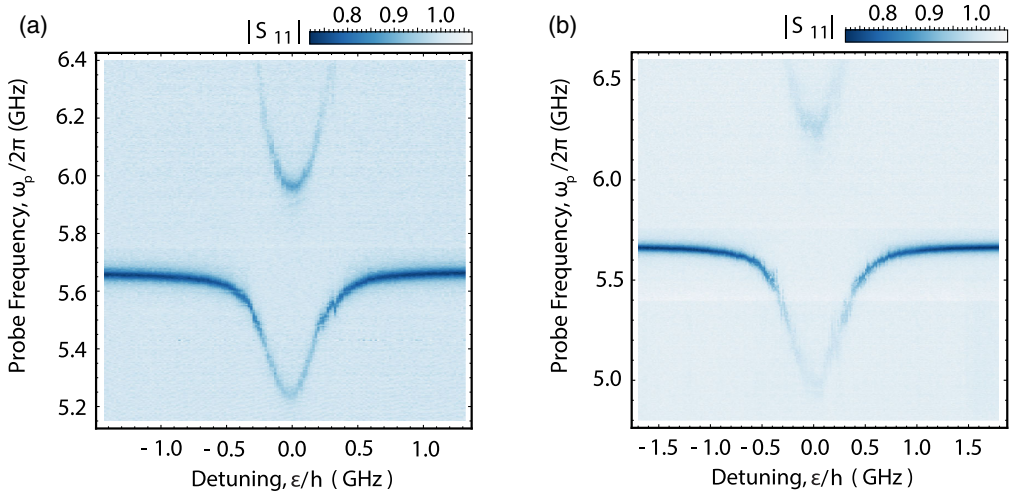

FIG. 13. Response of the Josephson-junction array resonator reflectance amplitude $|S_{11}|$ versus DQD detuning ϵ in correspondence of a DQD configuration characterized by parameter (a) $\eta \sim 0.50 \pm 0.14$ and (b) $\eta \sim 0.72 \pm 0.08$. Data are already reported in Figs. 5(b) and 11(b).

[1] R. Hanson, L. P. Kouwenhoven, J. R. Petta, S. Tarucha, and L. M. K. Vandersypen, *Spins in Few-Electron Quantum Dots*, Rev. Mod. Phys. **79**, 1217 (2007).

[2] F. A. Zwanenburg, A. S. Dzurak, A. Morello, M. Y. Simmons, L. C. L. Hollenberg, G. Klimeck, S. Rogge, S. N. Coppersmith, and M. A. Eriksson, *Silicon Quantum Electronics*, Rev. Mod. Phys. **85**, 961 (2013).

[3] L. M. K. Vandersypen, H. Bluhm, J. S. Clarke, A. S. Dzurak, R. Ishihara, A. Morello, D. J. Reilly, L. R. Schreiber, and M. Veldhorst, *Interfacing Spin Qubits in Quantum Dots and Donors—Hot, Dense, and Coherent*, npj Quantum Inf. **3**, 34 (2017).

[4] W. G. van der Wiel, S. De Franceschi, J. M. Elzerman, T. Fujisawa, S. Tarucha, and L. P. Kouwenhoven, *Electron Transport through Double Quantum Dots*, Rev. Mod. Phys. **75**, 1 (2002).

[5] G. Scappucci, C. Kloeffel, F. A. Zwanenburg, D. Loss, M. Myronov, J.-J. Zhang, S. De Franceschi, G. Katsaros, and M. Veldhorst, *The Germanium Quantum Information Route*, Nat. Rev. Mater. **6**, 926 (2021).

[6] T. Frey, P. J. Leek, M. Beck, A. Blais, T. Ihn, K. Ensslin, and A. Wallraff, *Dipole Coupling of a Double Quantum Dot to a Microwave Resonator*, Phys. Rev. Lett. **108**, 046807 (2012).

[7] K. D. Petersson, L. W. McFaul, M. D. Schroer, M. Jung, J. M. Taylor, A. A. Houck, and J. R. Petta, *Circuit Quantum Electrodynamics with a Spin Qubit*, Nature (London) **490**, 380 (2012).

[8] A. J. Landig, J. V. Koski, P. Scarlino, U. C. Mendes, A. Blais, C. Reichl, W. Wegscheider, A. Wallraff, K. Ensslin, and T. Ihn, *Coherent Spin-Photon Coupling Using a Resonant Exchange Qubit*, Nature (London) **560**, 179 (2018).

[9] X. Mi, J. V. Cady, D. M. Zajac, P. W. Deelman, and J. R. Petta, *Strong Coupling of a Single Electron in Silicon to a Microwave Photon*, Science **355**, 156 (2017).

[10] A. Stockklauser, P. Scarlino, J. V. Koski, S. Gasparinetti, C. K. Andersen, C. Reichl, W. Wegscheider, T. Ihn, K. Ensslin, and A. Wallraff, *Strong Coupling Cavity QED with Gate-Defined Double Quantum Dots Enabled by a High Impedance Resonator*, Phys. Rev. X **7**, 011030 (2017).

[11] L. E. Bruhat, T. Cubaynes, J. J. Viennot, M. C. Dartiailh, M. M. Desjardins, A. Cottet, and T. Kontos, *Circuit QED with a Quantum-Dot Charge Qubit Dressed by Cooper Pairs*, Phys. Rev. B **98**, 155313 (2018).

[12] X. Mi, M. Benito, S. Putz, D. M. Zajac, J. M. Taylor, G. Burkard, and J. R. Petta, *A Coherent Spin-Photon Interface in Silicon*, Nature (London) **555**, 599 (2018).

[13] N. Samkharadze, G. Zheng, N. Kalhor, D. Brousse, A. Sammak, U. C. Mendes, A. Blais, G. Scappucci, and L. M. K. Vandersypen, *Strong Spin-Photon Coupling in Silicon*, Science **359**, 1123 (2018).

[14] O. E. Dial, M. D. Shulman, S. P. Harvey, H. Bluhm, V. Umansky, and A. Yacoby, *Charge Noise Spectroscopy Using Coherent Exchange Oscillations in a Singlet-Triplet Qubit*, Phys. Rev. Lett. **110**, 146804 (2013).

[15] J. Yoneda, K. Takeda, T. Otsuka, T. Nakajima, M. R. Delbecq, G. Allison, T. Honda, T. Kodera, S. Oda, Y. Hoshi, N. Usami, K. M. Itoh, and S. Tarucha, *A Quantum-Dot Spin Qubit with Coherence Limited by Charge Noise and Fidelity Higher than 99.9%*, Nat. Nanotechnol. **13**, 102 (2018).

[16] K. D. Petersson, J. R. Petta, H. Lu, and A. C. Gossard, *Quantum Coherence in a One-Electron Semiconductor Charge Qubit*, Phys. Rev. Lett. **105**, 246804 (2010).

[17] D. Vion, A. Aassime, A. Cottet, P. Joyez, H. Pothier, C. Urbina, D. Esteve, and M. H. Devoret, *Manipulating the Quantum State of an Electrical Circuit*, Science **296**, 886 (2002).

[18] B. M. Maune, M. G. Borselli, B. Huang, T. D. Ladd, P. W. Deelman, K. S. Holabird, A. A. Kiselev, I. Alvarado-Rodriguez, R. S. Ross, A. E. Schmitz, M. Sokolich, C. A. Watson, M. F. Gyure, and A. T. Hunter, *Coherent Singlet-Triplet Oscillations in a Silicon-Based Double Quantum Dot*, Nature (London) **481**, 344 (2012).

[19] J. Medford, J. Beil, J. M. Taylor, E. I. Rashba, H. Lu, A. C. Gossard, and C. M. Marcus, *Quantum-Dot-Based Resonant Exchange Qubit*, Phys. Rev. Lett. **111**, 050501 (2013).

[20] J. Medford, J. Beil, J. M. Taylor, S. D. Bartlett, A. C. Doherty, E. I. Rashba, D. P. DiVincenzo, H. Lu, A. C. Gossard, and C. M. Marcus, *Self-Consistent Measurement and State Tomography of an Exchange-Only Spin Qubit*, Nat. Nanotechnol. **8**, 654 (2013).

[21] B. Thorgrimsson, D. Kim, Y.-C. Yang, L. W. Smith, C. B. Simmons, D. R. Ward, R. H. Foote, J. Corrigan, D. E. Savage, M. G. Lagally, M. Friesen, S. N. Coppersmith, and M. A. Eriksson, *Extending the Coherence of a Quantum Dot Hybrid Qubit*, npj Quantum Inf. **3**, 32 (2017).

[22] M. Benito and G. Burkard, *Hybrid Superconductor-Semiconductor Systems for Quantum Technology*, Appl. Phys. Lett. **116**, 190502 (2020).

[23] P. Scarlino, D. J. van Woerkom, A. Stockklauser, J. V. Koski, M. C. Collodo, S. Gasparinetti, C. Reichl, W. Wegscheider, T. Ihn, K. Ensslin, and A. Wallraff, *All-Microwave Control and Dispersive Readout of Gate-Defined Quantum Dot Qubits in Circuit Quantum Electrodynamics*, Phys. Rev. Lett. **122**, 206802 (2019).

[24] T. Niemczyk, F. Deppe, H. Huebl, E. P. Menzel, F. Hocke, M. J. Schwarz, J. J. Garcia-Ripoll, D. Zueco, T. Hümmer, E. Solano, A. Marx, and R. Gross, *Circuit Quantum Electrodynamics in the Ultrastrong-Coupling Regime*, Nat. Phys. **6**, 772 (2010).

[25] A. Frisk Kockum, A. Miranowicz, S. De Liberato, S. Savasta, and F. Nori, *Ultrastrong Coupling between Light and Matter*, Nat. Rev. Phys. **1**, 19 (2019).

[26] P. Forn-Díaz, L. Lamata, E. Rico, J. Kono, and E. Solano, *Ultrastrong Coupling Regimes of Light-Matter Interaction*, Rev. Mod. Phys. **91**, 025005 (2019).

[27] E. Paladino, Y. Galperin, G. Falci, and B. Altshuler, *1/f Noise: Implications for Solid-State Quantum Information*, Rev. Mod. Phys. **86**, 361 (2014).

[28] G. Ithier, E. Collin, P. Joyez, P. J. Meeson, D. Vion, D. Esteve, F. Chiarello, A. Shnirman, Y. Makhlin, J. Schriefl, and G. Schön, *Decoherence in a Superconducting Quantum Bit Circuit*, Phys. Rev. B **72**, 134519 (2005).

[29] A. Wallraff, D. I. Schuster, A. Blais, L. Frunzio, R.-S. Huang, J. Majer, S. Kumar, S. M. Girvin, and R. J. Schoelkopf, *Strong Coupling of a Single Photon to a Superconducting Qubit Using Circuit Quantum Electrodynamics*, Nature (London) **431**, 162 (2004).

[30] The total dissipation of the SQUID array resonator is not constant as a function of the resonator frequency due to the presence of standing waves in its microwave feedline.

[31] D. I. Schuster, A. Wallraff, A. Blais, L. Frunzio, R.-S. Huang, J. Majer, S. M. Girvin, and R. J. Schoelkopf, *ac Stark Shift and Dephasing of a Superconducting Qubit Strongly Coupled to a Cavity Field*, Phys. Rev. Lett. **94**, 123602 (2005).

[32] These measurements are implemented by changing the resonator frequency for performing these experiments in the dispersive regime, ensuring a negligible contribution of the Purcell induced decay ($\Gamma_{\mathrm{purcell}}/2\pi < 0.05$ MHz). Also, we drive the resonator weakly so that its population on average is < 1 photon. The reflected signal is then amplified via a Josephson parametric amplifier with a gain of approximately 18 dB.

[33] J. Q. You, X. Hu, and F. Nori, *Correlation-Induced Suppression of Decoherence in Capacitively Coupled Cooper-Pair Boxes*, Phys. Rev. B **72**, 144529 (2005).

[34] From unpublished data, reported in Fig. 10(a) in Appendix H, which is the topic of another manuscript, we observe an unexpected linear dependence of the coupling strength g on the resonator frequency $\omega_r(=\omega_q)$ measured at the sweet spot, $\epsilon = 0$. We take this into account by defining the normalized coupling $\bar{g}_\perp$ instead of the expected $\bar{g}'_\perp \propto \sqrt{\omega_r}$ dependence.

[35] A. Cottet, M. C. Dartiailh, M. M. Desjardins, T. Cubaynes, L. C. Contamin, M. Delbecq, J. J. Viennot, L. E. Bruhat, B. Douçot, and T. Kontos, *Cavity QED with Hybrid Nanocircuits: From Atomic-like Physics to Condensed Matter Phenomena*, J. Phys. Condens. Matter **29**, 433002 (2017).

[36] N. A. Masluk, I. M. Pop, A. Kamal, Z. K. Minev, and M. H. Devoret, *Microwave Characterization of Josephson Junction Arrays: Implementing a Low Loss Superinductance*, Phys. Rev. Lett. **109**, 137002 (2012).

[37] Figure 11 in Appendix Extra data reports the same analysis performed on a second DQD configuration characterized by $\eta \sim 0.5$. There, we obtain comparable results from fits to the Rabi and JC models.

[38] P. Scarlino, D. J. van Woerkom, U. C. Mendes, J. V. Koski, A. J. Landig, C. K. Andersen, S. Gasparinetti, C. Reichl, W. Wegscheider, K. Ensslin, T. Ihn, A. Blais, and A. Wallraff, *Coherent Microwave-Photon-Mediated Coupling between a Semiconductor and a Superconducting Qubit*, Nat. Commun. **10**, 3011 (2019).

[39] J. Basset, D.-D. Jarausch, A. Stockklauser, T. Frey, C. Reichl, W. Wegscheider, T. M. Ihn, K. Ensslin, and A. Wallraff, *Single-Electron Double Quantum Dot Dipole-Coupled to a Single Photonic Mode*, Phys. Rev. B **88**, 125312 (2013).

[40] D. J. van Woerkom, P. Scarlino, J. H. Ungerer, C. Muller, J. V. Koski, A. J. Landig, C. Reichl, W. Wegscheider, T. Ihn, K. Ensslin, and A. Wallraff, *Microwave Photon-Mediated Interactions between Semiconductor Qubits*, Phys. Rev. X **8**, 041018 (2018).

[41] D. J. Ibberson, T. Lundberg, J. A. Haigh, L. Hutin, B. Bertrand, S. Barraud, C.-M. Lee, N. A. Stelmashenko, G. A. Oakes, L. Cochrane, J. W. A. Robinson, M. Vinet, M. F. Gonzalez-Zalba, and L. A. Ibberson, *Large Dispersive Interaction between a CMOS Double Quantum Dot and Microwave Photons*, PRX Quantum **2**, 020315 (2021).

[42] D. de Jong, J. van Veen, L. Binci, A. Singh, P. Krogstrup, L. P. Kouwenhoven, W. Pfaff, and J. D. Watson, *Rapid Detection of Coherent Tunneling in an In-As Nanowire Quantum Dot through Dispersive Gate Sensing*, Phys. Rev. Applied **11**, 044061 (2019).

[43] M. Lodari, N. Hendrickx, W. Lawrie, T.-k. Hsiao, L. Vandersypen, A. Sammak, M. Veldhorst, and G. Scappucci, *Low Percolation Density and Charge Noise with Holes in Germanium*, Mater. Quantum. Technol. **1**, 011002 (2021).

[44] F. N. Froning, L. C. Camenzind, O. A. van der Molen, A. Li, E. P. Bakkers, D. M. Zumbühl, and F. R. Braakman, *Ultrafast Hole Spin Qubit with Gate-Tunable Spin-Orbit Switch Functionality*, Nat. Nanotechnol. **16**, 308 (2021).

[45] E. Kawakami, P. Scarlino, D. R. Ward, F. R. Braakman, D. E. Savage, M. G. Lagally, M. Friesen, S. N. Coppersmith, M. A. Eriksson, and L. M. K. Vandersypen, *Electrical Control of a Long-Lived Spin Qubit in a Si/SiGe Quantum Dot*, Nat. Nanotechnol. **9**, 666 (2014).

[46] J. Combes, J. Kerckhoff, and M. Sarovar, *The SLH Framework for Modeling Quantum Input-Output Networks*, Adv. Phys. X **2**, 784 (2017).

[47] C. Müller, J. Combes, A. R. Hamann, A. Fedorov, and T. M. Stace, *Nonreciprocal Atomic Scattering: A Saturable, Quantum Yagi-Uda Antenna*, Phys. Rev. A **96**, 053817 (2017).

[48] A. Rosario Hamann, C. Müller, M. Jerger, M. Zanner, J. Combes, M. Pletyukhov, M. Weides, T. M. Stace, and A. Fedorov, *Nonreciprocity Realized with Quantum Nonlinearity*, Phys. Rev. Lett. **121**, 123601 (2018).

[49] P. Harvey-Collard, G. Zheng, J. Dijkema, N. Samkharadze, A. Sammak, G. Scappucci, and L. M. K. Vandersypen, *On-Chip Microwave Filters for High-Impedance Resonators with Gate-Defined Quantum Dots*, Phys. Rev. Applied **14**, 034025 (2020).

[50] X. Mi, J. V. Cady, D. M. Zajac, J. Stehlik, L. F. Edge, and J. R. Petta, *Circuit Quantum Electrodynamics Architecture for Gate-Defined Quantum Dots in Silicon*, Appl. Phys. Lett. **110**, 043502 (2017).